

© 2020 American Physical Society. Access to this work was provided by the University of Maryland, Baltimore County (UMBC) ScholarWorks@UMBC digital repository on the Maryland Shared Open Access (MD-SOAR) platform.

Please provide feedback Please support the ScholarWorks@UMBC repository by emailing scholarworks-group@umbc.edu and telling us what having access to this work means to you and why it's important to you. Thank you.

Janus $\text{PtX}_n\text{Y}_{2-n}$ ($X, Y = \text{S, Se, Te}; 0 \leq n \leq 2$) Monolayers for Enhanced Photocatalytic Water Splitting

F. Ersan^{1,2,*} and C. Ataca^{2,†}¹*Department of Physics, Aydın Adnan Menderes University, 09100 Aydın, Turkey*²*Department of Physics, University of Maryland, Baltimore County, 1000 Hilltop Circle, Baltimore, Maryland 21250, USA*

(Received 30 January 2020; accepted 9 April 2020; published 3 June 2020)

We investigate Janus and alloy structures of $\text{PtX}_n\text{Y}_{2-n}$ ($X, Y = \text{S, Se, Te}; 0 \leq n \leq 2$) materials on the basis of first-principles plane-wave simulations. Using cluster-expansion theory to study alloys of $\text{PtX}_n\text{Y}_{2-n}$ monolayers at various concentrations, for half coverage ($n = 1$), our results indicate that Janus-type structures are not energetically the most favorable for PtXY monolayers; however, they are dynamically and thermally stable. To distinguish Janus PtXY structures, we report the Raman-active modes and compared them with those of bare PtX_2 monolayers. The electronic band gaps calculated with use of hybrid functionals are on par with available experimental data. Spin-orbit coupling significantly modifies the electronic band structure of PtXY monolayers. Because of the electronegativity differences of different chalcogen atoms on each surface of Janus PtXY structures, the arising dipole moment significantly modifies the band alignments on both surfaces. We find that hydrogen-evolution and oxygen-evolution reactions occur on different surfaces and that applied strain enhances the catalytic activity. We also investigate the monovacancy and stacking effects on the electronic properties of PtX_2 and PtXY structures. Our results indicate that due to their intrinsic dipole moments and band gaps, Janus PtXY monolayers are perfect candidates for water-splitting reactions.

DOI: [10.1103/PhysRevApplied.13.064008](https://doi.org/10.1103/PhysRevApplied.13.064008)

I. INTRODUCTION

Two-dimensional (2D) atomic layer structures, such as graphene, group III-V composites, phosphorene, and transition-metal dichalcogenides (TMDs), at the quantum-confinement limit are emerging as an important class of nanomaterials for novel applications in information technology, optoelectronics, spintronics, energy storage, and conversion technologies. [1–4] These materials are not only significantly different from their bulk counterparts but also display unusual properties due to the much-enhanced quantum confinement in two dimensions and their high surface-to-volume ratios. [5,6] TMDs with the chemical formula MX_2 (M is a transition-metal atom and X is a group-6A atom) have layered-type structures in their bulk phases. In general, intralayer interactions are of the weak van der Waals (vdW) type, while interlayer binding between M and X atoms is by strong chemical bonding [7]. This bonding type makes it possible to obtain low-dimensional MX_2 structures by mechanical exfoliation methods.

Two-dimensional materials have a wide range of structural, thermal, chemical, optical, magnetic, electrical, and mechanical properties that are otherwise unattainable and thus 2D materials present a unique opportunity in condensed-matter research and semiconductor devices. For instance, many MX_2 structures show indirect band gap to direct band gap transformation or they change to being a semiconductor from a metal when the dimensionality is reduced from the bulk to two dimensions, which makes them potential candidates for next-generation devices such as transistors [8], solar cells [9], and optoelectronic devices [10]. MoS_2 , MoSe_2 , and WS_2 monolayers (MLs) can absorb up to 5%–10% of incident sunlight, which is equivalent to the absorption rate of 50-nm-thick silicon slab used in current solar-cell technology [9]. Monolayer MoS_2 has been calculated to have a lower Li-ion-diffusion energy barrier and superior lithium-storage capacity in comparison with graphene [11]. Electronic, magnetic, or optical properties of TMDs can be tuned by applying strain and creating impurity defects such as vacancies, adatom adsorptions, or substitutions [12,13]. Another feasible method of tuning optoelectronic properties of TMDs includes ordered-disordered alloying [14]. Shi *et al.* [15] showed that $\text{Mo}(\text{S}_{1-x}\text{Se}_x)_2$ and $\text{Mo}_{1-y}\text{W}_y\text{S}_2$ have greater visible-light absorption than the

*fatih.ersan@adu.edu.tr

†ataca@umbc.edu

bare structures. Gan *et al.* [16] investigated the changing of the band gap in $\text{Mo}_{1-x}\text{W}_x\text{X}_2$ ($X = \text{S}, \text{Se}, \text{Te}$) and reported that the band gap does not change linearly with the alloying concentration, x . The band gap dipped around an alloying concentration of $x = 1/3$. Experimental investigations proved that few-layer $\text{MoS}_{2(1-x)}\text{Se}_{2x}$ alloy has greater hydrogen-evolution activity compared with pristine few-layer MoS_2 and MoSe_2 [17].

Recently, a different kind of TMD alloy, which is called a “Janus structure” was synthesized [18]. In Janus monolayers, even though transition-metal atoms are still sandwiched between chalcogen atoms, the chalcogen atoms on both sides are not identical. To synthesize Janus Mo-based structures, experimentalists prepared triangular MoS_2 monolayer flakes on sapphire substrates and then stripped off the top-layer sulfur atoms using a hydrogen plasma to obtain MoSH structures. By thermal selenization of the structure for the substrate temperature below 450°C , Janus MoSSe monolayers were obtained. A similar method was used by Zhang *et al.* [19], in which a Janus MoSSe monolayer was synthesized from a MoSe_2 monolayer. They obtained it by replacing the top layer of selenium atoms with sulfur atoms by controlled sulfurization of MoSe_2 . Er *et al.* [20] theoretically predicted that Janus WSSe monolayers have a higher hydrogen-evolution reaction rate with S or Se vacancies present in the system. Ji *et al.* [21] reported that Janus MoXY ($X, Y = \text{O}, \text{S}, \text{Se}, \text{Te}$) structures have an intrinsic dipole, which causes an internal electric field in the Janus MoXY monolayer. This results in electrons and holes accumulating on different surfaces of the Janus structures and enhances the photocatalytic reactivity for water splitting. Meng *et al.* [22] reported that a defective MoSSe monolayer can induce a magnetic moment under external strain. Biaxial strain can increase the n -type or p -type Seebeck coefficient of the Janus monolayer, and so does the power factor [23]. Compressive strain can enhance the anisotropic Rashba spin splitting in Janus MoXY and WXY monolayers [24]. While group-III monochalcogenide monolayers have piezoelectric coefficients of around 1–2 pm/V, these coefficients at least quadruple in the Janus counterparts, which makes them suitable materials for piezoelectric sensors and nanogenerators [25]. Recently Shi *et al.* [26] theoretically predicted many Janus monolayers of transition-metal dichalcogenides and many of them show a phase transition from semiconductor to metal. Janus TMD structures not only have enhanced electronic, magnetic, and chemical properties, but also have properties that are not present in the bare counterparts [27–29].

Platinum (Pt) nanoparticles are used intensively in direct methanol fuel cells and the hydrogen-evolution reaction (HER) due to their catalytic behavior [30–33]. Recently, the synthesis of monolayer PtSe_2 has revived interest in Pt-based dichalcogenides [34]. Chia *et al.* [35] focused on the electrocatalytic behavior of Pt-layered dichalcogenides

and reported that the hydrogen-evolution performance increases with decrease of the atomic number of the chalcogen atom. However, MoSe_2 is more efficient for hydrogen evolution compared with MoS_2 [36]. Sajjad *et al.* [37] investigated the optical properties of PtS_2 and PtSe_2 monolayers and found the exciton binding energies to be 0.78 and 0.60 eV, respectively. These exciton binding energies are lower than for $1H$ - MoS_2 (0.87 eV) and $1H$ - MoSe_2 (1.02 eV) [21]. While PtX_2 monolayers are nonmagnetic semiconductors, [38,39] hydrogen functionalization makes them ferromagnetic metals [40]. Zhang *et al.* [41] found that strain or Se-vacancy defects alone cannot induce magnetization in the PtSe_2 monolayer. Because of similar or superior properties, it is crucial to investigate the properties of Pt-based dichalcogenides and their Janus counterparts in detail.

In this study, using first-principles calculations, we investigate the structural, electronic, and vibrational properties of Janus-type Pt chalcogenides such as PtXY ($X, Y = \text{S}, \text{Se}, \text{Te}$). First, we investigate the dynamical stability and calculate the Raman-active frequencies for each PtXY . Second, we study the properties of Janus PtXY structures for energy and device applications such as efficient water-splitting photocatalysis and next-generation optoelectronic devices. We report the effects of biaxial strains and vacancy defects on the chemical, vibrational, electronic, and magnetic properties. Finally, we investigate possible alloys of $\text{PtX}_n\text{Y}_{2-n}$ structures with different concentrations (n) and find the ground states for each alloying ratio determine whether the Janus structures of PtXY are energetically favorable.

II. METHODS

Our simulations are based on first-principles spin-polarized plane-wave calculations within density-functional theory using projector-augmented-wave potentials [42]. The exchange-correlation functional is approximated by the generalized-gradient approximation with use of Perdew, Burke, and Ernzerhof (PBE) [43] and Heyd, Scuseria, and Ernzerhof (HSE) [44] functionals including vdW corrections at the D2 level [45]. To define the electron-electron interaction, the range separation is set to 0.2 \AA^{-1} and the AEXX which defines the fraction of exact exchange in a Hartree-Fock/DFT hybrid functional type calculation is set to 0.25. Wave functions are expanded in plane-wave basis sets up to an electron kinetic energy cut-off of 400 eV. Impurity and defects are modeled by a 4×4 periodic supercell in the x - y plane. To avoid interlayer interactions between consecutive primitive cells, a vacuum spacing of 20 Å is used (40 Å for the work-function calculations). Brillouin-zone integration is performed with an automatically generated $20 \times 20 \times 1$ k -point mesh following the convention of Monkhorst and Pack [46], and the k -point mesh is scaled accordingly for the supercell

simulations. Ionic relaxation to find the minimum energy of the structure is realized by the conjugated-gradient algorithm [47]. All atoms in the simulations are fully relaxed until the energy difference between the successive steps is less than 10^{-5} eV and the force on each atom is less than 10^{-2} eV/Å. In addition, the maximum pressure on the lattice is lowered to 0.1 kbar. Numerical calculations are performed with VASP [48,49]. To simulate different compositions, $\text{PtX}_n\text{Y}_{2-n}$ ($0 \leq n \leq 2$), we use the special-quasirandom-structures (SQS) [50] method that is implemented in the ATAT package [51]. For these calculations we use the primitive cells of PtX_2 and PtY_2 as initial structures for $n = 2$ and $n = 0$, respectively. To keep the cross-validation score for cluster-expansion calculations below 25 meV, we investigate more than 700 structures with different concentrations (n) for each $\text{PtX}_n\text{Y}_{2-n}$ structure. Thermal stability and desorption of specific structures are tested by *ab initio*, finite-temperature molecular-dynamics (MD) calculations. A Nosé thermostat is used, and Newton's equation of motion is integrated through the Verlet algorithm with time steps of 2 fs. All MD calculations are performed at 1000 K for 1000 iterations, which corresponds to 2 ps. Self-consistent-field calculations of the work functions and electronic energy bands corresponding to the optimized structures are performed with and without spin-orbit coupling (SOC).

The cohesive energy per atom of PtX_2 and Janus PtXY structures, $E_{\text{coh}} = [E_T(\text{free}) - E_T(\text{PtX}_n\text{Y}_{2-n})]/3$, is obtained by subtracting the total energy of the 2D structures, $E_T(\text{PtX}_n\text{Y}_{2-n})$, from the sum of the total energies (E_T) of the constituent free atoms (Pt, S, Se, Te), $E_T(\text{free}) = E_T(\text{Pt}) + n \times E_T(X) + (2 - n) \times E_T(Y)$. By definition, $E_{\text{coh}} > 0$ indicates binding. The defect-formation energies of the structures are obtained by the equation $E_{\text{form}} = E_{\text{defective}} + \mu_{\text{atom}} - E_{\text{bare}}$, where $E_{\text{defective}}$ and E_{bare} are the total energies of the PtX_2 or Janus PtXY structures with and without a defect, respectively, and μ_{atom} is the chemical potential of the atom subtracted to form a vacancy in the structures. We calculate the chemical potentials, μ_{atom} , of Pt, S, Se, and Te atoms to compute the defect-formation energy. For these calculations we use bulk platinum, selenium, and tellurium structures and sulfur gas (S_2).

III. RESULTS AND DISCUSSION

A. Structural properties and stability calculations

Stable PtX_2 ($X = \text{S}, \text{Se}, \text{Te}$) structures belong to space group $P\bar{3}m1$ with Pt atoms in octahedral coordination. This atomic geometry is also named the “1T phase” of TMDs. ML forms of PtX_2 are obtained by our increasing the layer-layer distances to more than 20 Å to inhibit layer-layer interaction. Figure 1 shows the optimized top and side views of the ML PtX_2 structure. To obtain Janus PtXY ($X, Y = \text{S}, \text{Se}, \text{Te}$), chalcogen atoms on the same side of ML

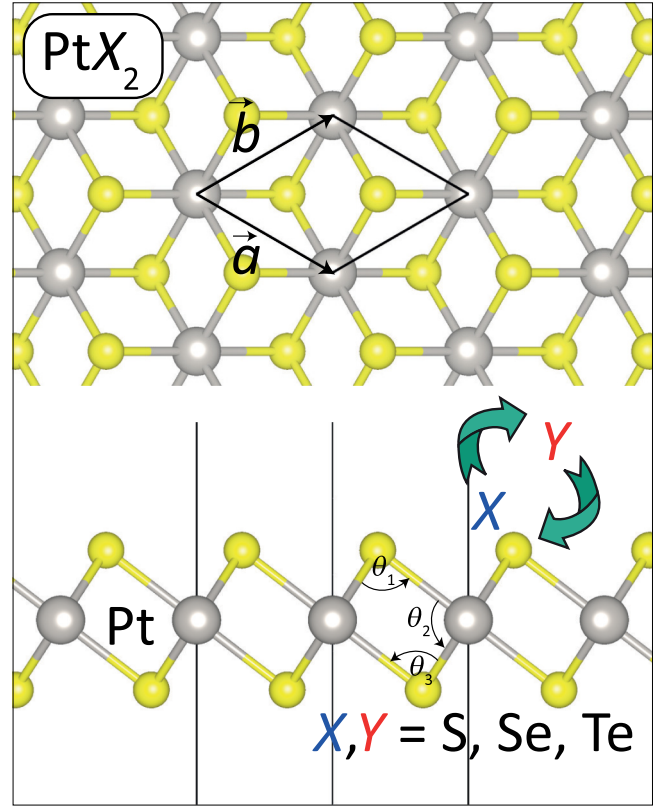


FIG. 1. Top view (top) and side view (bottom) of atomic structure of PtX_2 monolayers. Pt atoms are sandwiched between chalcogen atoms (X). Gray and yellow balls indicate platinum and chalcogen atoms ($X, Y = \text{S}, \text{Se}, \text{Te}$), respectively. Janus PtXY structures are obtained by our replacing X atoms in the same layer by Y chalcogen atoms. Lattice vectors are indicated by a and b in the primitive cell. $M-X-M$, $X-M-Y$, and $M-Y-M$ bond angles are labeled by θ_1 , θ_2 , and θ_3 , respectively.

are replaced with a different chalcogen atom as indicated by the arrows in the bottom part of Fig. 1.

Table I provides the structural parameters, including the lattice parameters, bond lengths and angles, cohesive energies, in-plane stiffness, and Poisson's ratio. The calculated lattice constants of the Janus PtXY structures are almost the average of those of PtX_2 and PtY_2 MLs. This can be thought of as applying $\pm 3\%$ strain if X and Y are neighbors in the periodic table or $\pm 5\%$ strain (for PtSTe) to bare MLs. The platinum-chalcogen bond lengths increase with increasing atomic number of the chalcogen atom. Even though the structure is different for Janus PtXY MLs, the Pt-chalcogen bond lengths vary slightly compared with those for bare MLs and this can be attributed to strain effects.

The first step in stability analysis is to calculate the cohesive energy of the structures. According to our definition in Sec. II, positive values indicate stability. Following similar trends as for the lattice parameters and bond lengths, the cohesive energies of bare and Janus MLs reported in Table I are all positive. In comparison with

TABLE I. Structural parameters and relevant energies calculated (PBE functional) for the stable monolayer PtX_2 and Janus PtXY : lattice constant (a); bond length in 2D monolayer structure [the first value is for the Pt–light-chalcogen bond length ($d_{\text{Pt-X}}$) and the second one is for the Pt–heavy-chalcogen bond length ($d_{\text{Pt-Y}}$); bond angles (θ) in the order $\theta_1, \theta_2, \theta_3$, which are depicted in Fig. 1; cohesive energy in the 2D monolayer structure (E_c); in-plane stiffness ($C_{x=y}$); and Poisson's ratio ($\nu_{xy} = \nu_{yx}$).

	PtS_2	PtSe_2	PtTe_2	PtSSe	PtSTe	PtSeTe
a (Å)	3.57	3.70	3.92	3.63	3.75	3.81
$d_{\text{Pt-X}} (\text{Y})$ (Å)	2.40	2.52	2.69	2.43, 2.50	2.48, 2.62	2.57, 2.64
Bond angle, θ (deg)	83.9, 96.1	85.6, 94.4	86.5, 93.5	93.3, 84.8, 97.0	97.9, 85.4, 91.1	92.3, 86.1, 95.5
E_{coh} (eV/atom)	4.71	4.45	4.31	4.56	4.43	4.36
$C_{x=y}$ (N/m)	98.4	88.1	68.5	92.6	77.5	75.8
$\nu_{xy} = \nu_{yx}$	0.291	0.306	0.262	0.298	0.294	0.304

calculated cohesive energies of other ML TMD structures [7], the amplitudes are smaller. Further analysis must be considered to ensure stability. Secondly, simulations are performed to investigate the mechanical properties of PtX_2 and PtXY structures. We calculate the in-plane stiffness [52] $C_{x,y} = (1/A) \partial E_T^2 / \partial \epsilon_{x,y}^2$ and Poisson's ratio $\nu_{xy} = \epsilon_y / \epsilon_x$ where, the unit-cell area is defined as A , the total energy per cell of the PtX_2 or PtXY structure is defined as E_T , and the applied uniaxial strain along the x (y) axis is defined as ϵ_x (ϵ_y). Because of equivalent in-plane lattice constants due to the symmetry of the structure, we find that $C_x = C_y$ and $\nu_{xy} = \nu_{yx}$. The calculated values listed in Table I indicate that the in-plane stiffness of the PtX_2 structures gets smaller on going from PtS_2 to PtTe_2 ; however, PtXY in-plane stiffness values are the average of the values of the constituent bare phases. Energy landscapes for $\pm 2\%$ uniaxial strains are illustrated in Appendix and the change of relative energy with applied uniaxial strain is shown in Fig. 2. The Pt-based MLs are in the elastic deformation region at the reported strain values. We apply more tensile

strain compared with compressive strain, since most materials become unstable when compressive strain is applied [53,54], while experimentally tensile strain can be up to 6% [55,56]. One can relate the in-plane stiffness of a material to its ability to withstand external mechanical effects. When compared with the other TMD MLs [7], Pt-based TMDs have lower Young's modulus values. They might not be suitable for mechanical device applications or functionalization such as membranes [57]. In addition, PtX_2 monolayers are stable in the 1T phase, so their piezoelectric constants are lower than those of 1H-phase TMDs [58,59]. However, because of the broken in-plane and out-of-plane symmetries in Janus PtXY monolayers, the piezoelectric constants are significantly increased [58].

To confirm the dynamical stability of the all the monolayer structures considered in the present study, we obtain phonon dispersion curves using the density-functional-perturbation-theory method (using a $5 \times 5 \times 1$ supercell) with PHONOPY [60]. The phonon band structures obtained and their corresponding partial phonon density of states are illustrated in Fig. 3. There are three atoms in each unit cell of the crystal structures, so there are nine vibrational modes, of which three are acoustic modes and six are optical modes. As shown in Fig. 3, the vibration frequencies of all PtX_2 and PtXY structures are positive in the whole Brillouin zone. As the mass of the constituent atoms increases, the vibration frequencies of the acoustic and optical modes decrease. In addition, the highest optical vibrational modes originate from S atoms in the PtS_2 or PtSY (Janus) structures, while for other structures they originate from a mixture of Pt and lighter chalcogen atoms. Heavier chalcogen atoms contribute to lower-frequency optical modes.

Because of the breaking of the centrosymmetry between the two chalcogen layers in Janus-ML PtXY structures, the point symmetry of the structure changes from $\bar{3}m$ in ML PtX_2 to $3m1$ in Janus-ML PtXY , which implies the number of symmetry operators reduces to 6 from 12. This results in a change of the irreducible representations at the Γ high-symmetry point from $\Gamma = 2E_g + A_{1g} + 4E_u + 2A_{2u}$ to $\Gamma = 2E'_g + A'_{1g} + 4E'_u + 2A'_{2u}$. While bare ML PtX_2 structures have only one E_g Raman mode

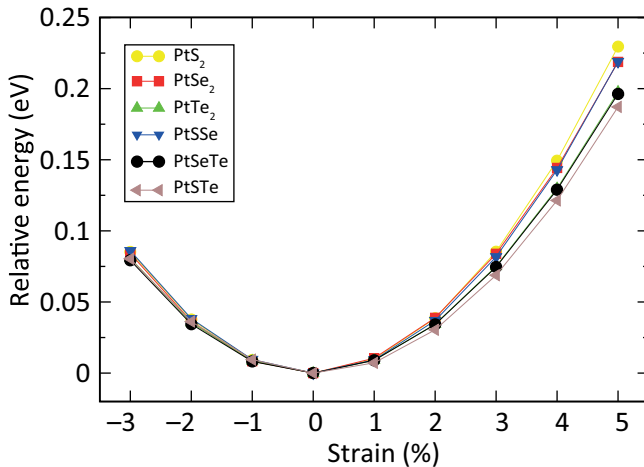


FIG. 2. Effects of applied strain on the total energy of the unit cell of bare PtX_2 and Janus PtXY structures. Energies are reported relative to the ground-state energy of the PBE-functional calculations. Different shapes and colors represent different atomic formulas as are indicated in the legend.

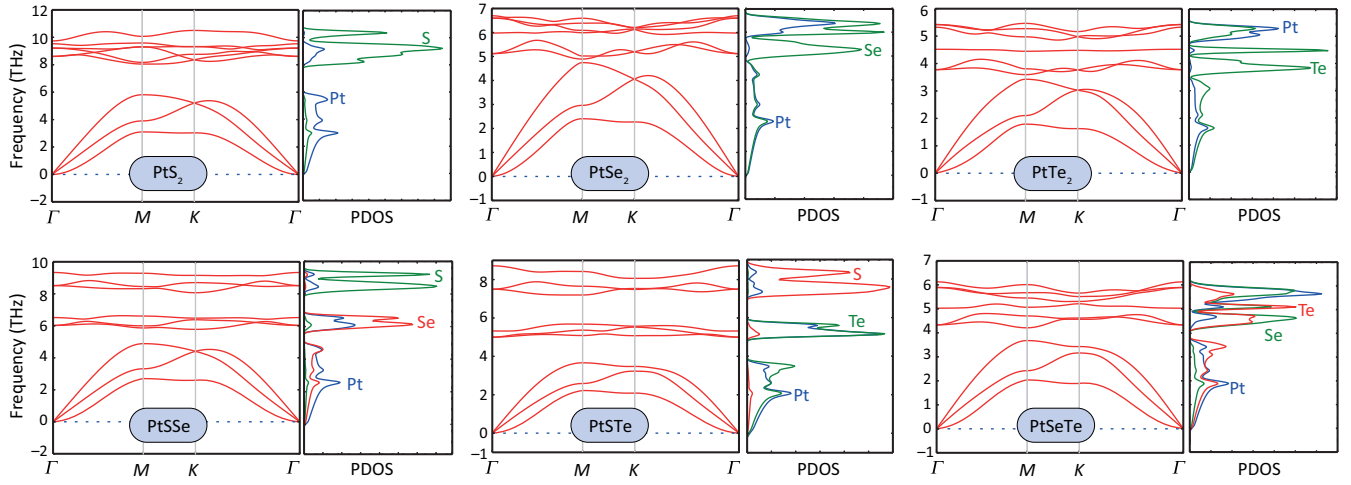


FIG. 3. Phonon band structure (PBE-functional calculation) along high-symmetry points on the left and projected density of states on Pt and chalcogen atoms on the right for each bare PtX_2 (upper row) and Janus PtXY structure (lower row).

and one A_{1g} Raman mode, the Janus-ML PtXY structures have two additional modes (E'_u and A'_{2u}). The theoretically calculated Raman-active modes and their corresponding atomic movements and frequencies are shown in Fig. 4 for ML PtX_2 and Janus-ML PtXY structures. More-detailed information on the Raman spectra and the corresponding intensities is reported in Appendix. Increase of the heavier atomic number in the Janus PtXY structures results a decrease of the E'_u -mode intensity and this mode almost disappears for PtSeTe (the calculated intensity is negligible).

B. Electronic properties of PtX_2 and PtXY structures

The electronic band structures and corresponding band-decomposed charge densities for specific k points are obtained for the equilibrium (strain-free) ML PtX_2 and Janus-ML PtXY structures with use of the HSE functional including SOC and they are shown in Fig. 5. All of the MLs considered have an indirect band gap. Even though this

band-gap character is independent of the functional used in density-functional-theory simulations or inclusion of spin-orbit coupling (PBE functional, HSE functional, PBE functional plus SOC, HSE functional plus SOC), the band gaps significantly depend on the functional. The calculated band gaps for different functionals with and without SOC effects are given in Table II. The calculated band gaps for the Janus PtXY structures are almost the average of the band gaps of the bare PtX_2 structures. Spin-orbit coupling is less effective for bare PtS_2 (40 meV for the PBE functional, 38 meV for the HSE functional), but its effects increase as heavier chalcogen atoms are introduced in the ML structure (e.g., for PtTe_2 the band-gap difference is 327 meV for the PBE functional and 426 meV for the HSE functional). These SOC effects are also dominant for the Janus structures containing heavy chalcogen atoms (Se or Te) in one of their surfaces (the SOC effect on the band gap ranges between 160 and 340 meV).

To understand the orbital contribution to the valence-band maximum (VBM) and the conduction-band minimum (CBM), band-decomposed charge densities are also given in Fig. 5. For the bare PtX_2 MLs, the VBMs are dominated by the p orbitals of chalcogen atoms, while the CBMs are dominated by the p orbitals of chalcogen atoms and the d orbitals of the Pt atoms. Our PBE-functional and HSE-functional calculations excluding SOC effects show that there are degenerate bands at the VBM at the Γ high-symmetry point for all structures considered and these are dominated totally by p orbitals of the chalcogen atoms. However, spin-orbit interaction splits these degenerate bands, leaving the VBM dominated by the p_{xy} orbitals of the chalcogens, pushing the chalcogens' p_z orbitals to lower energy levels. In addition, SOC is effective also in d orbitals of the Pt atom. Normally, d orbitals of the metal atoms split into twofold e_g (d_{z^2} , $d_{x^2-y^2}$) and

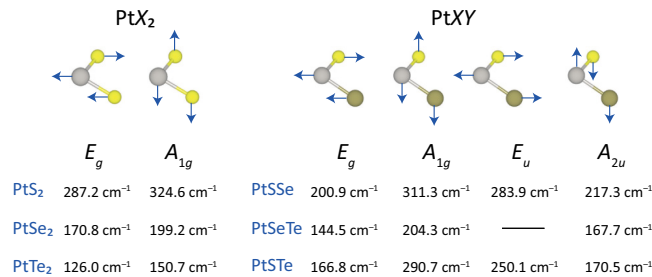


FIG. 4. Raman-active modes, corresponding atomic movements, and frequencies for ML PtX_2 and Janus-ML PtXY structures (PBE-functional calculation). Yellow, light-gray, and dark-gray balls represent, light-chalcogen, platinum, and heavy-chalcogen atoms, respectively.

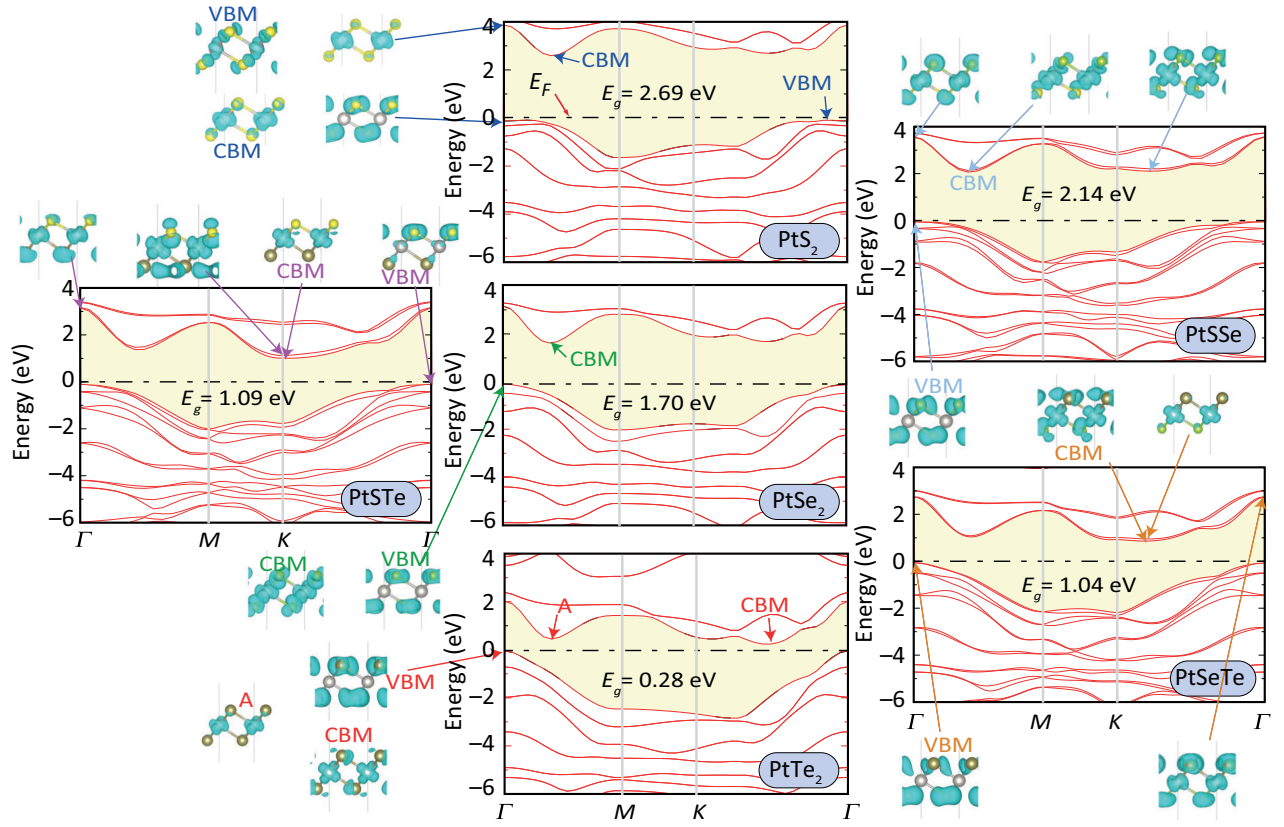


FIG. 5. Electronic band structure of ML PtX_2 and Janus-ML PtXY structures calculated with the HSE functional including spin-orbit coupling. The Fermi level, E_F , is set at 0 eV and is indicated by dashed black lines for each structure. All of the ML structures have indirect band gaps and their amplitude is given by E_g for each structure. Band-decomposed charge densities for specific k points shown by arrows are indicated. Isosurface values for charge densities are taken as $0.0001 \text{ eV}/\text{\AA}^3$.

threefold t_{2g} (d_{xy} , d_{yz} , d_{xz}) orbitals; however, the SOC further splits the e_g and t_{2g} orbitals into e_1 (d_{xz} , d_{yz}), e_2 (d_{xy} , $d_{x^2-y^2}$), and a_1 (d_{z^2}) orbitals. All CBMs of the MLs considered are dominated by e_1 orbitals of the Pt atoms and the p_{xy} orbitals of the chalcogen atoms. One major difference of Janus PtXY MLs from bare MLs is that the dominant p_{xy} -orbital contribution at the VBM of the Janus PtXY MLs comes from the light chalcogen atoms and not an equally from both chalcogen layers as in the case of bare MLs.

Since both the CBM and the VBM are heavily dependent on the p_{xy} orbitals of all MLs studied, it is crucial to study the effects of strain on the electronic band structure and the charge transfer between transition-metal and chalcogen atoms. The variation of the band gaps (direct and indirect band gaps) of bare PtX_2 and Janus PtXY structures obtained with the HSE functional with spin-orbit interaction as a function of compressive and tensile strain is illustrated in Fig. 6. Our calculations show that the indirect-band-gap character of the MLs considered is unchanged in the strain-ratio range from -3% to 5% . However, the energy difference between the direct and indirect band gaps decreases with increasing tensile strain and vice versa for the compressive strain. For example, this

band-gap difference is 120 meV for the equilibrium PtS_2 ML and is 30 meV for 5% tensile strain, while it is calculated as 320 meV for -3% compressive strain. Applying compressive strain always decreases the electronic band gap for the all MLs considered and even makes PtTe_2 metallic at around 2%–3% compressive strain.

Figure 7 illustrates the variation of charge transfer as a function of the applied strain. For structures without Te as a chalcogen layer, there is a minor charge-transfer difference between Pt and chalcogen layers. The main reason why the direct and indirect electronic band gaps converge as shown in Fig. 6 is because of the significant modification on the valence bands. As the applied strain increases, the first two degenerate bands of PtS_2 and PtSe_2 and first four bands of PtSSe shift energetically toward lower values. The gap is no longer from the Γ point in the valence band to the Γ -M midpoint in conduction band, and it becomes a direct gap from the same k -point at the CBM. (sixth band from the VBM to the CBM as indicated in Fig. 5) The new VBM is dominated by the p_z orbitals of S and/or Se atoms, which is the main difference from Te-based MLs.

In the case of Te-based ML structures, similar observations for the valence bands are also valid; however, the new

TABLE II. Fundamental band gaps of monolayer PtX_2 and Janus PtXY structures (E_g); charge transfer between the atoms ρ with positive sign indicating depletion of electrons from the atoms and negative sign indicating electron accumulation on the atoms; Born effective charges Z^* on the atoms; static dielectric constant $\epsilon_{\text{static}}^{aa,bb}$ including local field effects; electrostatic potential difference between the surfaces $\Delta\phi$; intrinsic dipole moment (d_μ); and H_2O adsorption energy for the monolayers considered (E_{ads}). In the first column, the physical property and the density-functional-theory functional used to obtain the reported values are given.

	PtS_2	PtSe_2	PtTe_2	PtSSe	PtSTe	PtSeTe
E_g (eV), PBE	1.81	1.34	0.43	1.56	0.85	0.83
E_g (eV), PBE + SOC	1.77	1.15	0.11	1.41	0.63	0.53
E_g (eV), HSE	2.78	1.88	0.72	2.28	1.32	1.26
E_g (eV), HSE + SOC	2.69	1.70	0.28	2.14	1.09	1.04
ρ (electrons), PBE	Pt 0.57 S -0.28	Pt 0.16 Se -0.08	Pt -0.50 Te 0.25	Pt 0.35 S -0.29 Se -0.06	Pt -0.03 S -0.32 Te 0.35	Pt -0.21 Se -0.12 Te 0.33
$Z_{a(b)}^*$, PBE	Pt 2.60 S -1.30	Pt 2.12 Se -1.06	Pt 0.94 Te -0.47	Pt 2.40 S -1.42 Se -0.98	Pt 2.04 S -1.99 Te -0.05	Pt 1.61 Se -1.55 Te -0.06
$\epsilon_{\text{static}}^{aa,bb}$, PBE	4.72	5.88	8.24	5.34	6.67	7.09
$\Delta\phi$ (eV), PBE, HSE + SOC	0	0	0	0.67, 0.75	1.45, 1.65	0.79, 0.92
d_μ (D), HSE + SOC	0	0	0	0.23	0.54	0.31
E_{ads} (meV), PBE	171	172	189	183	136	195

VBM is dominated by Te atoms' p_x and p_y orbitals, with a slight p_z -orbital contribution. The main difference for Te-based ML structures is the charge transfer between the three constituent layers of the materials. Tellurium acts as a cation layer providing electrons to Pt and other chalcogen layers as seen in Fig. 7. Platinum layers do not donate electrons but accumulate more electrons with increasing applied strain. This results in the lowering of the energy of the CBM since all structures considered are dominated by the Pt layer as shown in Fig. 5. For this reason the energy difference between the direct and indirect band gaps of Te-based ML structures decrease more than those of S-based and Se-based ML structures as the applied strain increases.

For the pristine PtX_2 monolayers, since both of the chalcogen layers are formed from the same atoms, there is

no resulting internal electric field due to the symmetry. In the case of Janus PtXY structures, where the chalcogen layers are formed from different atoms and charged differently due to the electronegativity difference between atoms or layers, the internal electric field between chalcogen layers results in an electrostatic potential difference between the top layer and the bottom layer of PtXY MLs. See Appendix for more details for the average potential for some structures. The calculated electrostatic potential difference ($\Delta\phi$) between two separated surfaces of the Janus PtXY structures (which also result in a dipole moment in Janus MLs) is given in Table II. With increase of the electronegativity differences between the surface atoms, the electrostatic potential difference increases. For example, $\Delta\phi = 0.75$ eV for PtSSe but increases to 1.65 eV for PtSTe . In addition

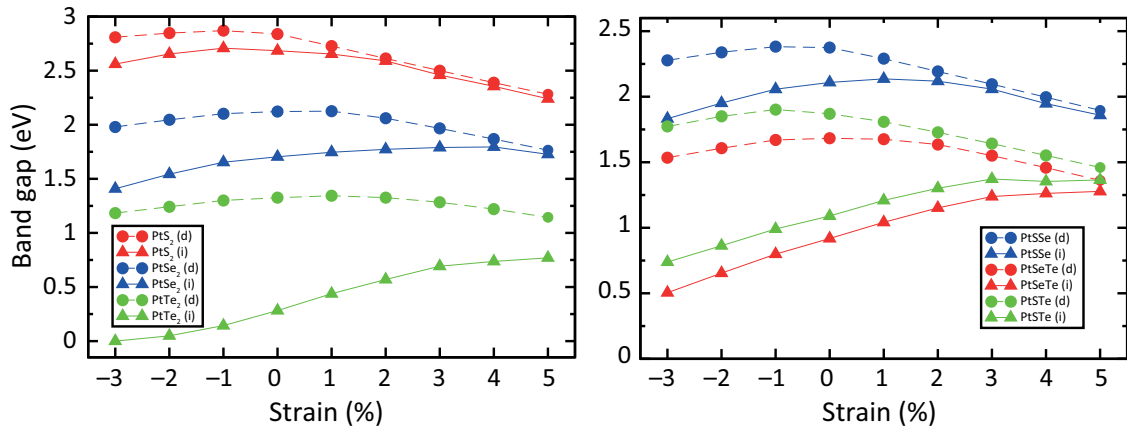


FIG. 6. Variation of indirect band gap (triangles) and direct band gap (circles) under applied biaxial strain for bare PtX_2 MLs on the left and Janus PtXY MLs on the right for HSE-functional calculations including SOC effects. Red, blue, and green represent PtS_2 (PtSeTe), PtSe_2 (PtSSe), and PtTe_2 (PtSTe), respectively.

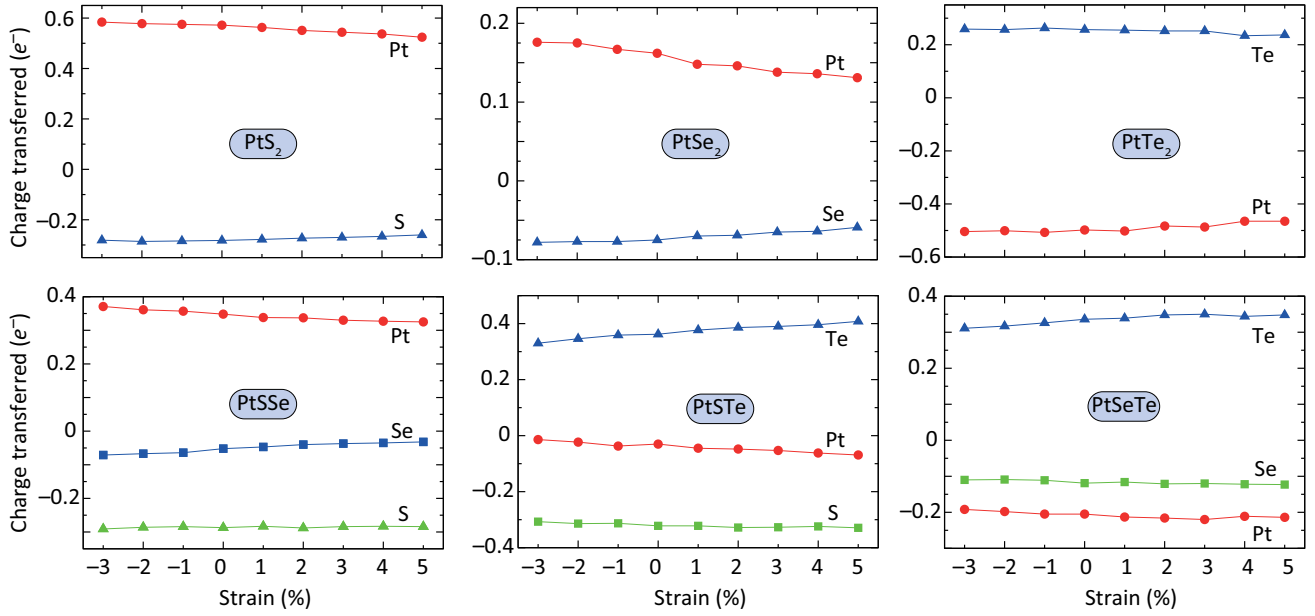


FIG. 7. Variation of charge transferred between transition-metal and chalcogen atoms under applied strain (PBE-functional calculation). Red, green, and blue lines indicate the charge state of transition-metal, lighter-chalcogen, and heavier-chalcogen atoms, respectively. For bare structures, chalcogen-atom total charge transferred is indicated by blue lines.

to the electrostatic potential difference between the X and Y surfaces, there is an intrinsic dipole moment. The dipole moments are given in Table II and increase with increase of the internal electric field.

Calculated Born effective charges for the in-plane direction ($Z_{a(b)}^*$) and static dielectric constants ($\epsilon_{aa,bb}^{\text{static}}$) which include local field effects are given in Table II. These results are obtained from density-functional-perturbation-theory calculations. The Born effective charge, Z^* , is defined as $eZ_{j\alpha\beta}^* = \Omega(\partial P_\alpha / \partial u_{j\beta})$, where Ω is volume of the unit cell and Z^* is the coefficient of proportionality between the change in field-induced electric polarization P in direction α arising from an atomic displacement u_j in direction β for zero external field ($E = 0$). The Born effective charge of Pt atoms in any ML structure is always positive, unlike in Bader charge analysis, and the Born effective charges on the chalcogen atoms decrease similarly with decreasing electronegativity of the atoms. Even though tellurium atoms' born effective charges are never positive as is the case in Bader charge analysis, in -based Janus MLs, the Te atoms' Born effective charges can be ignored. The static dielectric constants of Janus PtXY MLs are calculated to be very close to the average of the values of the constituent MLs, such as PtX_2 and PtY_2 .

C. Photocatalytic properties of PtX_2 and PtXY monolayer structures

To decompose pure water into hydrogen (H_2) and oxygen (O_2) molecules at 25°C , a standard potential of 1.23 V is required on the basis of the Nernst equation. The

corresponding standard reduction and oxidation potentials for H^+/H_2 and for OH^-/O_2 are -4.44 and -5.67 eV for $p\text{H } 0$, respectively [61]. However, the standard potential of 1.23 V remains unchanged with variation of the acidic ratio of water, but the reduction and oxidation potentials increase by 0.059 eV for every unitary increment of the $p\text{H}$ value of the environment [62]. For example, for $p\text{H } 7$, the reduction potential level is -4.027 eV, while the oxidation potential is -5.257 eV. If the band edges of the materials align closely to these critical values, these materials can be suitable for water-splitting applications. In other words, if the conduction band of the material is positioned higher than the hydrogen-reduction potential and the valence band of the material is positioned lower than the oxygen-evolution potential, this material is suitable both for the HER and for the oxygen-evolution reaction (OER) (type-1 material). If the material's band alignments are suitable for only the HER or the OER, it is called a type-2 material for the water-splitting reaction.

The energies of the valence-band maximum and conduction-band minimum of bare PtX_2 and Janus PtXY structures under applied strain are given in Fig. 8. Spin-orbit coupling and the electrostatic potential difference between the chalcogen atomic layers of Janus MLs are also included in the simulations. These effects play an important role in the calculation of the work function of a material that is chalcogen side dependent in Janus MLs. Table II reports the amplitude of the electrostatic potential difference for Janus MLs, and its effect on the vacuum level is indicated in Appendix. Previous studies

showed that bare PtS_2 , $PtSe_2$, and Janus $PtSSe$ have suitable band-edge positions for water splitting [58,63], which is consistent with our results. However, none of these studies included all possible Janus MLs with the effects of electrostatic potential difference, spin-orbit coupling, and strain.

Our simulations on bare PtX_2 MLs indicate that PtS_2 and $PtSe_2$ MLs are suitable for the HER or the OER when certain conditions are met. With increase of the tensile strain, the energies of the CBM of PtS_2 and $PtSe_2$ decrease. While the CBM of $PtSe_2$ reaches the critical energy of -4.44 eV, the CBM of PtS_2 becomes lower than that, and thus PtS_2 ML can not excite the electrons for water reduction. For $PtTe_2$ MLs even though the energy of the CBM is suitable (for strains greater than -1%) for the HER, the band gaps are lower than the required potential energy of 1.23 eV and the VBM energies are higher than desirable oxidation-potential levels. Thus, the bare $PtTe_2$ monolayer structure is unsuitable for water-splitting applications. The effects of SOC are more pronounced on the VBM edge energies of $PtSe_2$ and $PtTe_2$ MLs.

Janus $PtXY$ MLs open alternative possibilities for water-splitting applications. Since there is an electrostatic potential difference between the chalcogen layers due the

charge-transfer differences, both chalcogen layers have different CBM and VBM energy positions as indicated in Fig. 8. In the case of Janus $PtSSe$, band alignments indicate that (HSE functional plus SOC) the S side of the ML is suitable for the OER but not the HER, but the Se side is suitable for both reactions. The localized effects are more pronounced for $PtSTe$ and $PtSeTe$ MLs since the HER occurs only on the Te layers and the OER occurs on the other chalcogen layer. Thus electron-hole pairs created on absorption of photons travel to opposite sides of the material (holes to the light-chalcogen sides and electrons to the heavy-chalcogen side) and the HER and OER occur on the different surfaces of the Janus MLs (while water reduction can occur on the heavy-chalcogen side, oxidation can occur on the light-chalcogen side). This also enables the Janus MLs ($PtSTe$ and $PtSeTe$) to conduct the HER or the OER without requiring a band-gap potential energy of 1.23 eV, in agreement with the a proposed mechanism for water splitting [21,64]. The calculated band-edge positions are very dependent on the functional used (HSE, HSE plus SOC). For example, $PtSeTe$ structures including applied compressive and tensile strain are not suitable for water splitting according to simulations with the HSE functional without the SOC effect, while they are potential

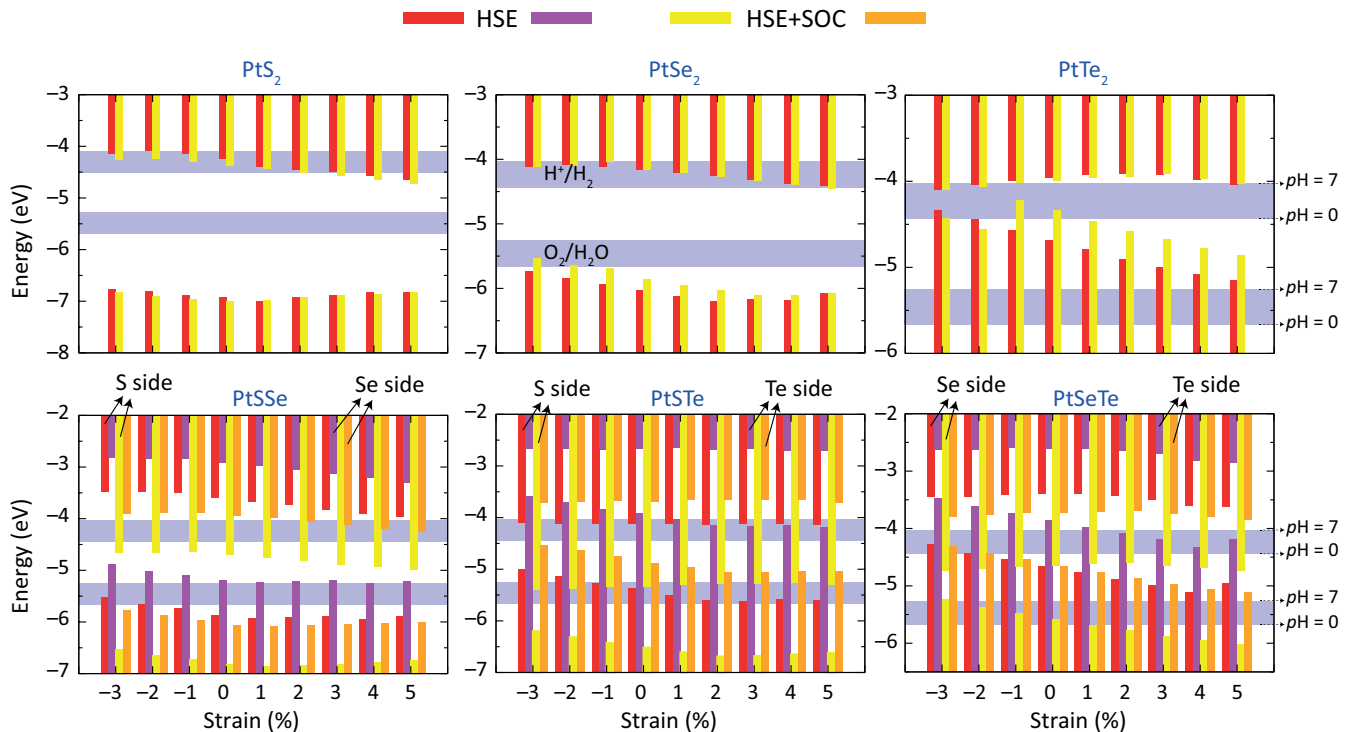


FIG. 8. Energies of valence-band maximum and conduction-band minimum of bare PtX_2 and Janus $PtXY$ MLs under applied strain. For bare MLs, red and yellow bars represent simulation results obtained with the HSE functional and with the HSE functional including spin-orbit interaction, respectively. For Janus MLs with an intrinsic dipole moment, red and purple bars represent energies calculated with the HSE functional on the lighter-chalcogen side and the heavier-chalcogen side, respectively. Yellow and orange bars have a similar meaning, but the energies are calculated with the HSE functional including spin-orbit interaction. Blue shaded regions represent possible potential values for the OER and the HER for various pH values.

photocatalysts in HSE functional simulations with SOC effects. Application of strain generally does not affect the CBM energies of Janus MLs containing Te as one of the chalcogen types. The VBM energies decrease on increase of the applied strain independently of the functional used in the simulations. In addition, the computed H₂O adsorption energies reported in Table II which indicates that there is physisorption between the water molecule and the surfaces of Janus MLs, which is a desirable result for water-splitting applications.

D. Vacancy and layer effects in PtX₂ and PtXY monolayer structures

Point defects such as atoms vacancies in the pristine crystal structure are the dominant defect types and can arise spontaneously in the crystal during the fabrication process. Therefore, to understand and benchmark the modifications in the electronic structure, we study monochalcogenide vacancy in the monolayer of PtX₂ and Janus PtXY structures. For these simulations we use a $4 \times 4 \times 1$ supercell to achieve sufficient defect-defect distance (at least 14 Å) and mimic the isolated point defect. We calculate that all defective supercells have the same lattice constants as their defect-free counterparts, which is further evidence of these monovacancies mimicking the local defects. Calculations for defective structures are performed using the PBE functional excluding SOC effects due to large supercells and the large number of electrons in the cells. Calculated defect-formation energies, fundamental band gaps and electrostatic potential differences are given in Table III.

The formation energy of the vacancy defect depends on the chalcogen atoms and increases on going from Te (Se) defects to Se (S) defects. There are two competing factors affecting the vacancy-formation energy [41]. These

are the applied strain ratio (creating defects requires less energy for the materials under strain) and charge transfer (the higher the charge transfer, the higher the formation energy). On this basis, one would expect that the vacancy-formation energy will be lower in Janus MLs than in bare PtX₂, and for the same Janus MLs, creating the defect on the heavier-chalcogen side will require less energy. The formation energies reported in Table III confirm this relation except for PtSeTe MLs. The energy for vacancy formation on the Te side of PtSeTe is higher than that for bare PtTe₂ because charge transfer in Janus MLs is greater than in bare MLs.

While perfect PtX₂ and Janus PtXY monolayers have indirect band gaps in the equilibrium and under applied strain, the creation of monochalcogenide vacancy converts all band structures to direct-band gap-character due to the localized defect states (see Appendix for the electronic band structures.). To understand how creating vacancy defects influences the electronic structure, we first focus on localized states at the VBM and the CBM of Janus structures. Localized states at the VBM and CBM originate from the dangling Pt—X or Pt—Y bonds. If we take the energy of the VBM as a reference, the energy of the CBM depends on two parameters. These are (i) the composition and geometric structure and (ii) the induced potential differences between surfaces. In Table II and Figs. 6 and 7, we report how the band gaps and charge transfers are influenced by the composition and applied strain. As the atomic number of the chalcogen atom increases, the band gap decreases, so the localized states (VBM and CBM) in the band-gap region will span narrower energy levels. In the case of X or Y vacancy in the PtXY monolayer, the position of the CBM depends on to what extent the chalcogen atom was withdrawing electrons from the structure. The greater the value, the farther away the localized state will

TABLE III. Formation energy E_{form} , fundamental band gaps of X -monovacancy monolayer PtX₂ and $X(Y)$ -monovacancy Janus PtXY structures (E_g), electrostatic potential difference between the surfaces $\Delta\phi$, interlayer binding energy of AA -stacked PtX₂ and PtXY bilayer structures ($E_{\text{binding}}^{\text{bilayer}}$) [the first energy values are computed by our subtracting the total energy of two monolayers from the bilayer's total energy of PtX₂ or PtXY [all calculations are performed with the vdW correction term], the second energy values are obtained by our considering vdW correction for only bilayers, while monolayer total energies are considered without vdW correction]; interlayer vertical distance (d_{bilayer}) of AA -stacked bilayers (with vdW correction), and fundamental band gaps of AA -stacked bilayer PtX₂ and AA -stacked bilayer Janus PtXY structures (E_g^{bilayer}). All calculations are performed with the PBE functional.

	PtS ₂	PtSe ₂	PtTe ₂	PtSSe	PtSTe	PtSeTe
E_{form} (eV)	3.45	2.74	2.27	S vacancy 3.43 Se vacancy 2.63	S vacancy 3.00 Te vacancy 2.14	Se vacancy 2.44 Te vacancy 2.40
E_g (eV)	0.81	0.57	0.29	S vacancy 0.54 Se vacancy 0.78	S vacancy 0.24 Te vacancy 0.57	S vacancy 0.40 Te vacancy 0.51
$\Delta\phi$ (eV)	0.07	0.06	0.01	S vacancy 0.72 Se vacancy 0.60	S vacancy 1.47 Te vacancy 1.35	Se vacancy 0.85 Te vacancy 0.76
$E_{\text{binding}}^{\text{bilayer}}$ (eV)	−0.20/−2.12	−0.55/−2.85	−0.71/−3.34	−0.54/−2.66	−0.76/−3.07	−0.70/−3.17
d_{bilayer} (Å)	2.08	2.14	2.32	2.12	2.17	2.22
E_g^{bilayer} (eV)	0.78	0.18	Semimetal	0.39	Semimetal	Semimetal

be from CBM of the bare structure (in other words, the lower the energy of the CBM in the defective structure, the less n -type doping due to the lack of a greater electron donor). Another important criterion we focus on is the splitting of the CBM around high-symmetry points. The energy difference due to the splitting is directly proportional to the enhancement or suppression of the electrostatic potential between the surfaces of the ML, $\Delta\phi$, after the defect creation. Creation of X vacancies increases $\Delta\phi$, whereas creation of Y vacancies decreases $\Delta\phi$ due to the difference in charge transfer. Combining both of these effects, one can conclude that (i) the band gap of defective PtX_2 and PtXY MLs will be lower as heavier chalcogen atoms are considered and (ii) for Janus structures only, lighter chalcogen atoms increase $\Delta\phi$ and thus reduce the band gap. These changes in the band gap will have an effect on the catalytic properties of materials: increased $\Delta\phi$ values will change the CBM and VBM energy levels and so a material that is not suitable for water splitting can be made suitable by these changes. Other point defects such as divacancy, antisite defect, or Stone-Wales defect can make a positive contribution to increase the catalytic properties of the Janus PtXY structures.

The effects of the number of layers in low-dimensional layered materials on the optoelectronic and magnetic properties are significant [65–67]; therefore, we investigated bilayers of the bare PtX_2 and Janus PtXY structures. For Janus PtXY bilayers, we consider three different stacking orders as AA , AB , and AC . The optimized bilayers are illustrated in Appendix. The calculated total energy of the structures shows that AA stacking order is energetically the most favorable for the Janus PtXY bilayers, while AB and AC stacking orders have the same total energies. The total energy difference between AA and AB (AC) stacking order for PtSSe is 78 meV, for PtSTe is 52 meV, and for PtSeTe is 82 meV. For this reason, we focus further only on AA stacking for all MLs.

We calculate the interlayer binding energy $E_{\text{binding}}^{\text{bilayer}}$ with the expression $E_{\text{binding}}^{\text{bilayer}} = E^{\text{bilayer}} - 2 \times E^{\text{monolayer}}$, where E^{bilayer} and $E^{\text{monolayer}}$ are the total energy of the bilayer and the monolayer of the structures considered. Two values are reported in Table III for $E_{\text{binding}}^{\text{bilayer}}$ due to inconsistency and totally different reported results in the literature [63]: first $E_{\text{binding}}^{\text{bilayer}}$ obtained with the vdW correction term for both bilayer and monolayer structures, and second $E_{\text{binding}}^{\text{bilayer}}$ obtained with the vdW correction term for only bilayer structures. As can be seen, there are huge differences between the two $E_{\text{binding}}^{\text{bilayer}}$ values; however, the second energies do not show the true layer-layer interaction between the layers, due to bilayer and monolayer structures having different input parameters for the calculation. See Appendix for more details of the bilayer PtX_2 and PtXY structures.

E. $\text{PtX}_n\text{Y}_{2-n}$ ($0 \leq n \leq 2$) monolayers

To discuss alloy $\text{PtX}_n\text{Y}_{2-n}$ structures and compare the energies of Janus PtXY alloys with other ordered or disordered alloys for $n = 1$, we perform density-functional-theory calculations within the cluster-expansion formalism [51]. The formation energy E_{form} (in electronvolts/atom) of $\text{PtX}_n\text{Y}_{2-n}$ alloy is defined as $E_{\text{form}} = [E_{\text{PtX}_n\text{Y}_{2-n}} - (n/2)E_{\text{PtX}_2} - (2 - n/2)E_{\text{PtY}_2}]/3$, where $E_{\text{PtX}_n\text{Y}_{2-n}}$, E_{PtX_2} , and E_{PtY_2} are the total energies of $\text{PtX}_n\text{Y}_{2-n}$, PtX_2 , and PtY_2 cells, all per formula unit. Formation-energy calculations for various concentrations of $\text{PtX}_n\text{Y}_{2-n}$ structures (Fig. 9) show that none of the alloy structures are energetically more favorable than the constituent bare PtX_2 monolayers. In the $\text{PtX}_n\text{Y}_{2-n}$ alloys for $n = 1$, Janus PtXY monolayers are energetically the least-favorable structures as indicated by the circles in Fig. 9. The energy differences between the favorable and Janus PtXY structures are 20 and 25 meV/atom for PtSSe and PtSeTe monolayers; however, the difference is 90 meV/atom for the PtSTe structure. This might be because surface tension between the S and Te layers due to lattice mismatch (between PtS_2 and PtTe_2) is greatest for Janus PtSTe . The energetically favorable configuration might be the curved or rolled configuration in the free-standing form. These energy differences indicate that Janus forms of PtXY MLs can be synthesized only in ambient conditions (such as temperature) and if they are placed on substrates. The best example for this situation is the synthesis of the Janus MoSSe structure [18,19]. As reported there, the substrate temperature is the most-important parameter and it must be kept constant and at a suitable value (450 °C) to avoid the formation of disordered MoSSe structures.

The crystal structures of the energetically favorable PtXY ($n = 1$) structures are indicated in insets in Fig. 9. Although it seems as if all PtXY structures have different ground states, there are many different PtXY structures around the minimum-energy region for $n = 1$, and they are separated from each other by only 3–5 meV/atom. Therefore, we focus on the energetically-most-favorable ones in further investigations. The bottom panels in the Fig. 9 show the total and atom projected density of states (PDOS) (obtained with the HSE functional with SOC effects) for the Janus and favorable PtXY monolayers. To make a comparison between them all, the PDOS are normalized to the formula unit of the PtXY structures. The favorable PtXY monolayers have slightly larger band gaps than the Janus forms. The main differences in then PDOS arise from the absence of the first peak around the VBM in the energetically favorable structures. For Janus PtXY MLs, these peaks originate from localized charges on X and Y layers, as indicated by the band-decomposed charge densities in Fig. 5. Because the energetically favorable PtXY monolayers have the same numbers of X atoms and Y atoms in their surfaces, the electrostatic potential differences between the

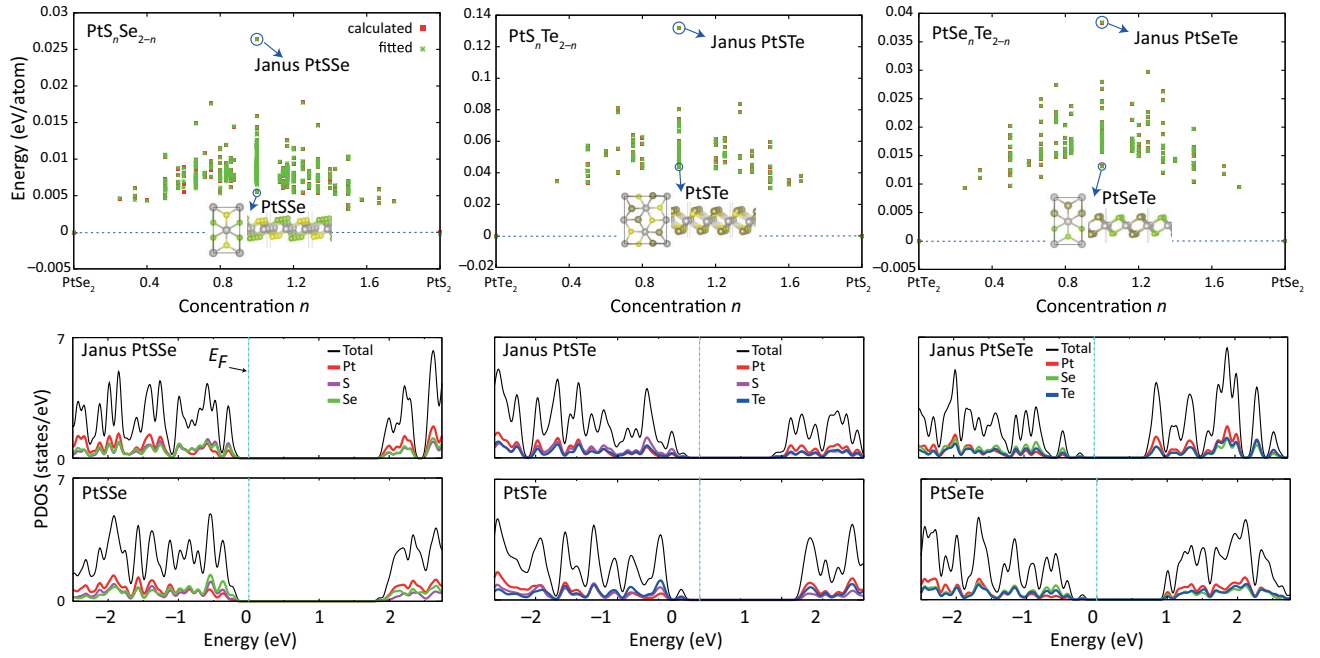


FIG. 9. Energies for alloying $\text{PtX}_n\text{Y}_{2-n}$ MLs at various concentrations are presented in the upper row (PBE-functional calculation). Janus PtXY structures are circled in blue and the geometric structure of the lowest-energy PtXY structure is indicated. The lower two rows show the PDOS for Janus PtXY structures (second row) and the energetically-most-favorable PtXY structures (third row). The Fermi level is set at 0 eV and is indicated by a dashed blue line. PDOS are obtained with HSE functional with inclusion of SOC effects.

surfaces diminish for these structures. The calculated band edges for the CBM and the VBM (considering vacuum-level energies) confirm that the favorable PtSSe monolayer has suitable band edges (CBM -6.36 eV and VBM -4.36 eV) for water splitting. However, PtSTe (CBM -5.46 eV and VBM -4.02 eV) monolayers and PtSeTe (CBM -5.26 eV and VBM -4.09 eV) monolayers can be used only for suitable $p\text{H}$ value water. On the basis of these results, Janus PtXY MLs are more suitable for water-splitting reactions.

IV. CONCLUSION

In summary, with our first-principles calculations, we predict Janus and alloy structures of $\text{PtX}_n\text{Y}_{2-n}$ ($X, Y = \text{S, Se, Te}$; $0 \leq n \leq 2$) materials. Cluster-expansion calculations show that Janus PtXY monolayers are energetically the least-favorable structures for half coverage ($n = 1$) of alloy $\text{PtX}_n\text{Y}_{2-n}$ monolayers; however, phonon and MD calculations indicate that they are stable. The calculated Raman-active modes for PtX_2 monolayers are in good agreement with the experimental results, so we believe that Raman-active frequencies obtained for Janus PtXY will benefit experimentalists when they try to synthesize these materials. Different electronegativity between the chalcogen atoms on each surface of the Janus PtXY monolayers gives rise to an intrinsic dipole moment and an internal electric field in monolayer PtXY pointing from

the heavy-chalcogen-atom surface to the light-chalcogen-atom surface. This dipole moment modifies the band alignments on both surfaces, and the HER and OER can occur on different surfaces of the Janus PtXY structures. Because Pt, Se, and Te atoms have a large number of electrons in d orbitals, SOC significantly modifies the electronic band structures and makes especially the Janus PtXTe monolayers suitable for water-splitting reactions. Our results indicate that because of their intrinsic dipole moments and band gaps, Janus PtXY monolayers are perfect candidates for water-splitting devices.

ACKNOWLEDGMENTS

Some of the calculations were performed at University of Maryland, Baltimore County High Performance Computing Facility and the TÜBİTAK ULAKBİM, High Performance and Grid Computing Center. This work was supported by the National Science Foundation through the Division of Materials Research under Grant No. DMR-1726213.

APPENDIX

In this appendix, we present the energy landscapes, Raman spectrums and corresponding vibrational modes, MD snapshots and difference charge densities of the PtX_2 and Janus PtXY monolayers. We also include the local potential profile of the monolayer bare and S-vacant PtS_2

and PtSSe structures along the z axis. Side views of the optimized atomic structure of the physisorbed water molecule on the monolayer PtX_2 and PtXY structures are illustrated in this appendix. In addition, electronic-energy-band structures are given for the single chalcogen vacancy included monolayers and defect-free bilayers of the PtX_2 and Janus PtXY structures.

Energy landscapes for $\pm 2\%$ uniaxial strains are illustrated in Fig. 10. By using these energy values and supplied strain ratio we calculated the in-plane stiffness and Poisson's ratio of the 2D PtX_2 and PtXY monolayers which are given in Table I.

The theoretically calculated Raman spectrum of bare PtX_2 and Janus PtXY monolayers and the corresponding

vibrational modes of Pt and X or Y atoms at the center of the Brillouin zone (Γ) are illustrated in Fig. 11. The most intense Raman mode for the bare PtX_2 monolayers is E_g which corresponds to Pt atoms moving in opposite directions parallel to the x -axis. For Janus PtXY monolayers the intensity of the E_g reduces and A_{2u} mode gets more intense. In addition, increase of the heavier atomic number in the Janus PtXY structures results a decrease of the E_u mode intensity and this mode almost disappears for PtSeTe (the calculated intensity is negligible).

We also perform temperature-dependent *ab initio* MD simulations (using a $5 \times 5 \times 1$ supercell) to study whether the stability can be maintained at elevated temperatures. We chose a microcanonical ensemble (number of particles,

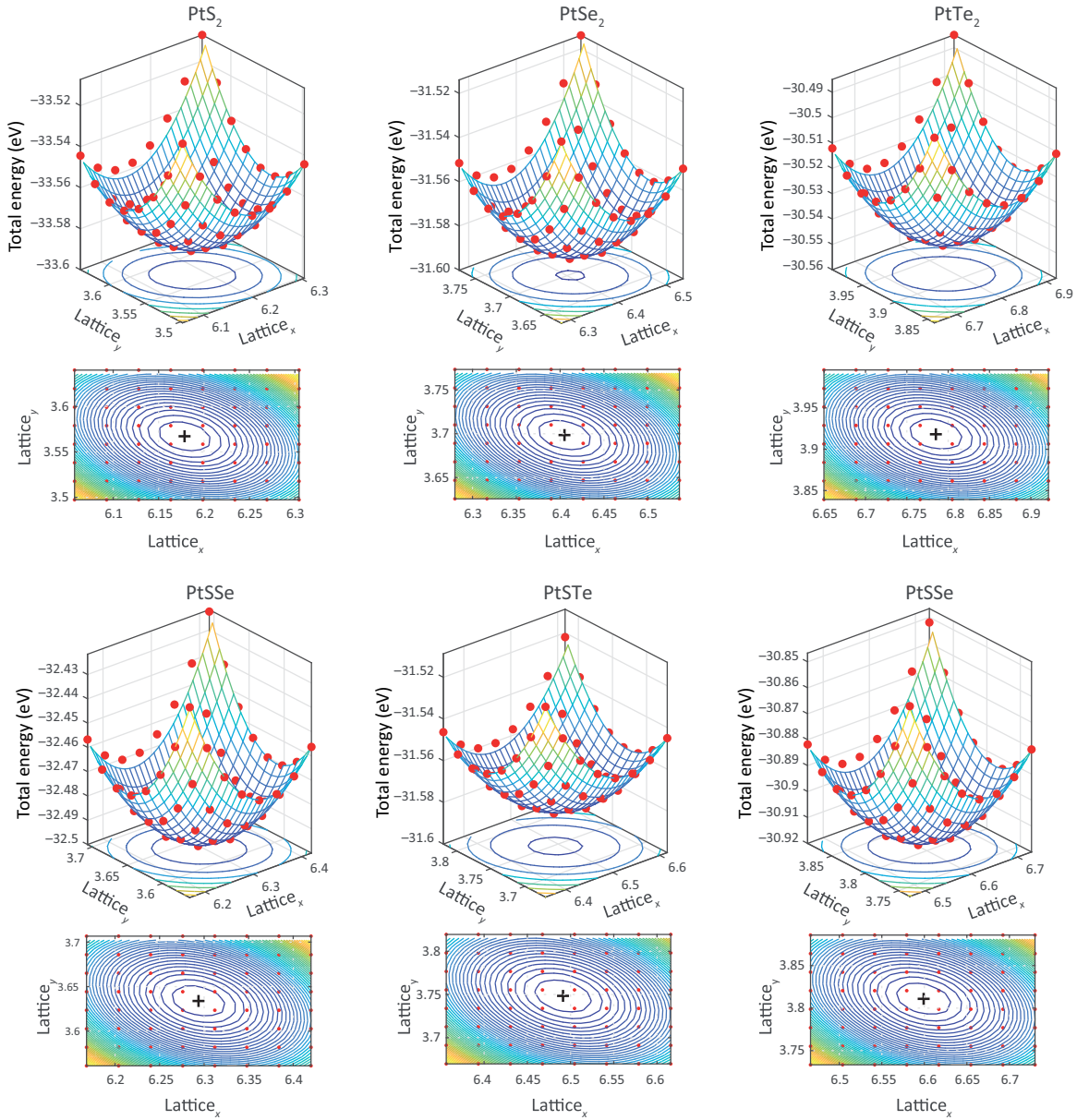


FIG. 10. Energy landscapes for the monolayer PtX_2 and PtXY structures (PBE-functional calculations).

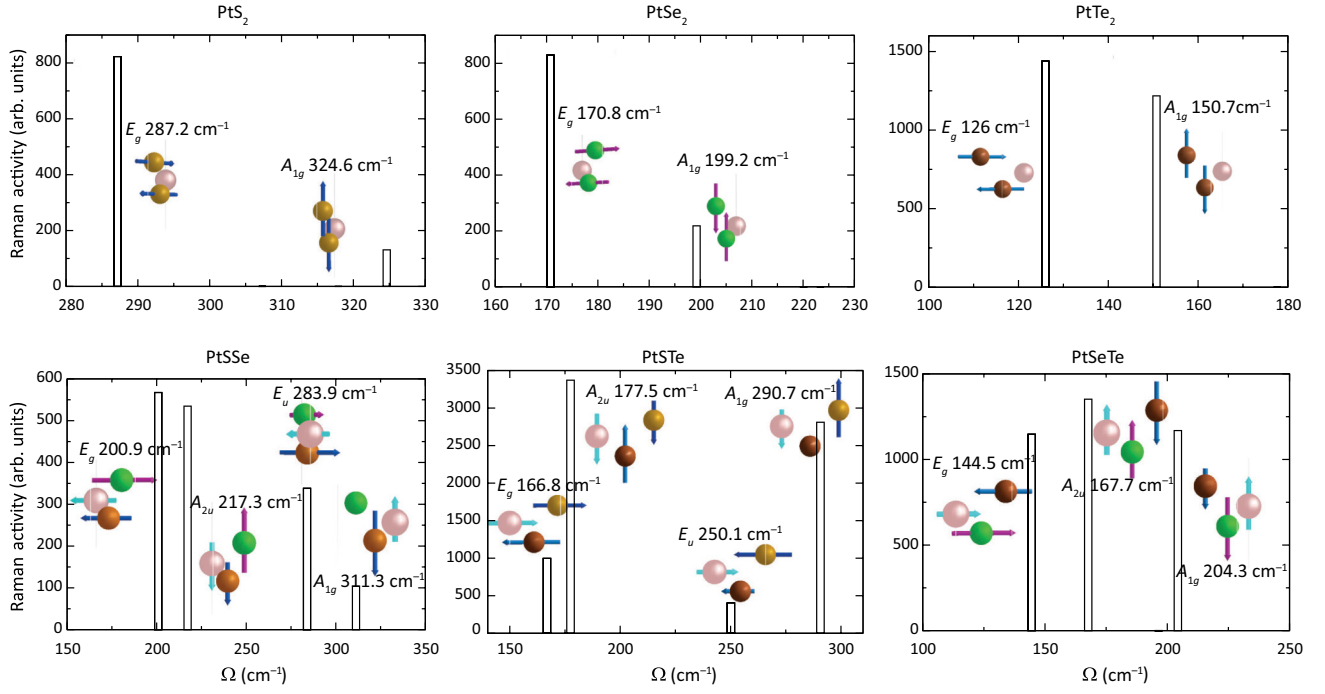


FIG. 11. Computed (PBE-functional calculations) Raman spectrum and corresponding vibrational modes for the monolayer PtX_2 and $PtXY$ structures. Pink, yellow, green, and red balls represent Pt, S, Se, and Te atoms, respectively.

volume and total energy are constant) with temperature set at 1000 K. Regular transition-metal dichalcogenides are not stable at such a temperature [7,18,19]. With a long time step of 2 fs for a total of 2 ps of total simulation time, these exaggerated simulation parameters favor instability. Snapshots of atomic configurations of the Janus $PtXY$ structures are illustrated in the Fig. 12. There is a little fluctuation in the structures but they remain stable.

Important information can be obtained from studying the charge transfer between transition-metal and chalcogen

layers to understand further the effects of strain. Charge-difference isosurfaces for all bare and Janus MLs are shown in Fig. 13 and the calculated charge transferred is given in Table II. The calculations indicate that electrons are transferred from Pt atoms to the S and Se atoms for bare PtS_2 , $PtSe_2$, and $PtSSe$ monolayers in accordance with the Pauli scale of electronegativity. Because platinum is more electronegative than Te, the charge transfer is reversed, Pt being the anion and Te being the cation. Unlike for S and Se atoms, the charge-difference isosurface plots in Fig. 13

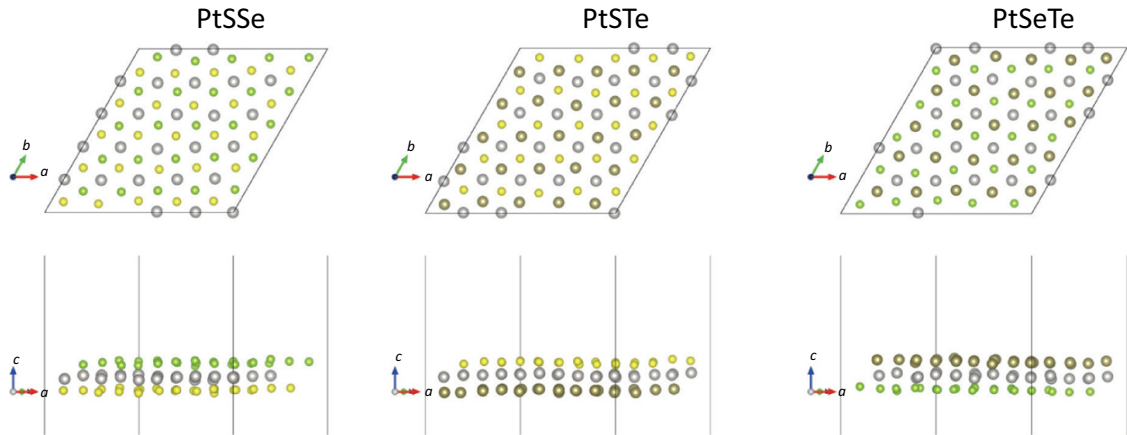


FIG. 12. Top and side views of the snapshots of the atomic configurations of the monolayer Janus $PtXY$ structures taken from MD simulations (PBE-functional calculations) performed at 1000 K for a total duration of 2 ps.

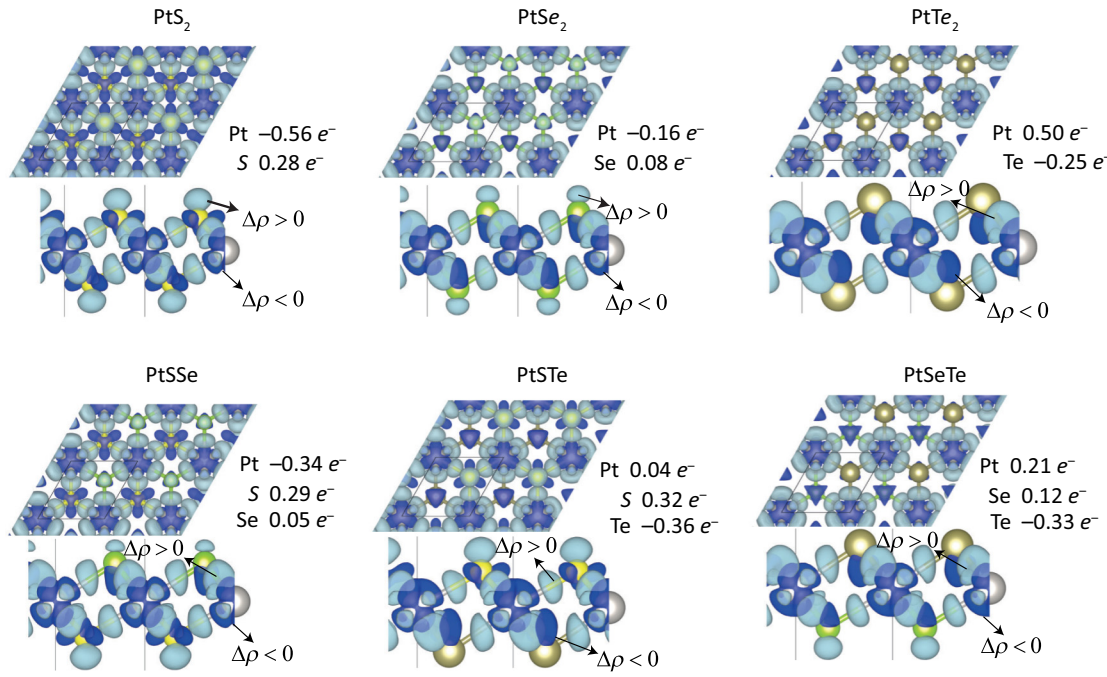


FIG. 13. Difference charge densities (PBE-functional calculations) for the monolayer PtX_2 and PtXY structures. Light blue indicates charge accumulation ($\Delta\rho > 0$), while dark blue indicates charge depletion ($\Delta\rho < 0$). $\Delta\rho = \rho_{\text{total}} - \rho_{\text{Pt}} - \rho_{\text{X,Y}}$.

show that the p_z orbitals of Te are not occupied in any bare and Janus MLs.

The variation of the average potentials for bare and S-vacant PtS_2 and PtSSe structures are given in Fig. 14. The calculated electrostatic potential difference for bare and S-vacant PtS_2 is zero. This may imply that low ratio vacancy defect is not effective on the electrostatic potential difference between two chalcogen layers. However, Janus PtSSe has high electrostatic potential difference between two separated chalcogen surfaces due to the electronegativity difference between the surface atoms.

Single water molecule initially placed 2 Å above the top site of the Pt atoms and released to the geometric optimization. Figure 15 indicates the optimized atomic structures of the water molecule adsorbed on bare PtX_2 and Janus PtXY structures. As can be seen after the optimization water molecule physisorbed on the structures are slightly tilted. This physisorption is a desirable result for water-splitting application.

Figure 16 illustrates the electronic-energy-band structures for the single chalcogen vacancy included in the monolayer PtX_2 and PtXY structures. We should note that,

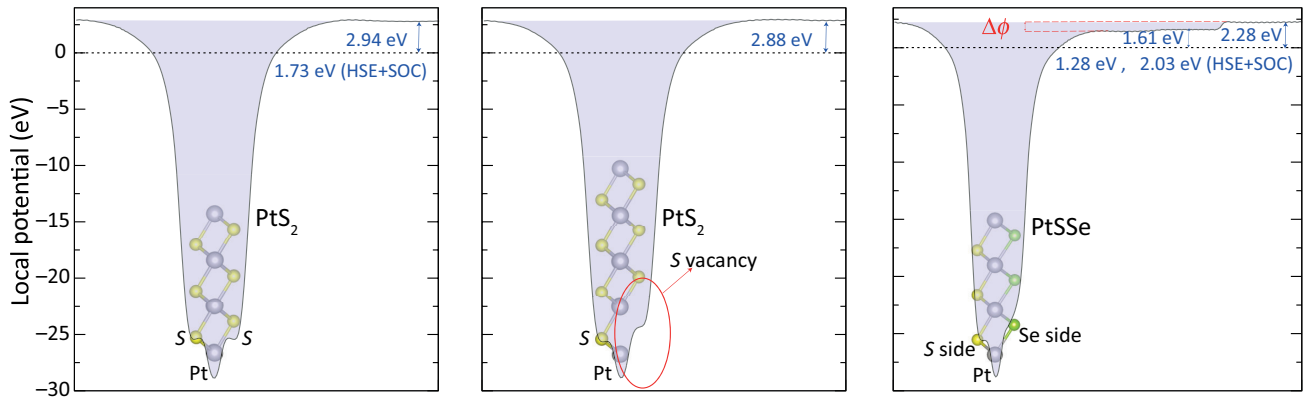


FIG. 14. Local potential profile of the monolayer bare and S-vacant PtS_2 and PtSSe structures along the z axis. The Fermi level is set to zero and corresponding atom potential wells are presented. The energy difference between the vacuum level and the Fermi level is calculated with the PBE functional and the HSE functional with SOC effects.

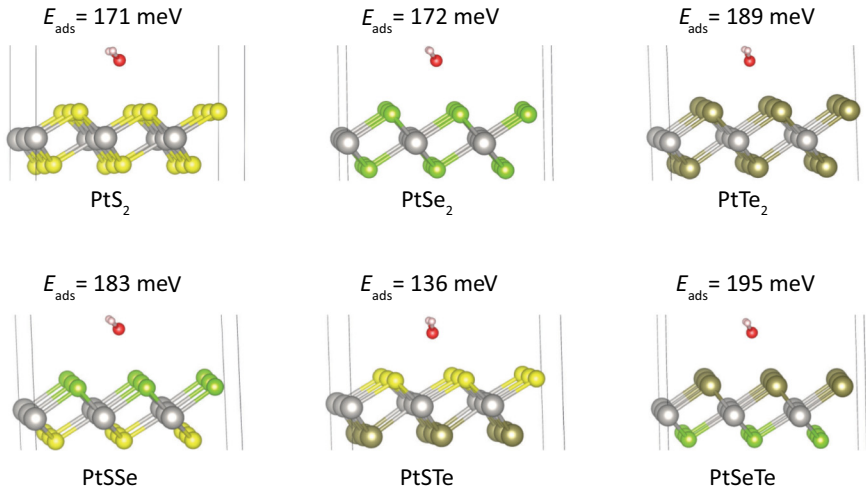


FIG. 15. Side views of the optimized atomic structure of the physisorbed water molecule on the monolayer PtX_2 and PtXY structures (PBE-functional calculations).

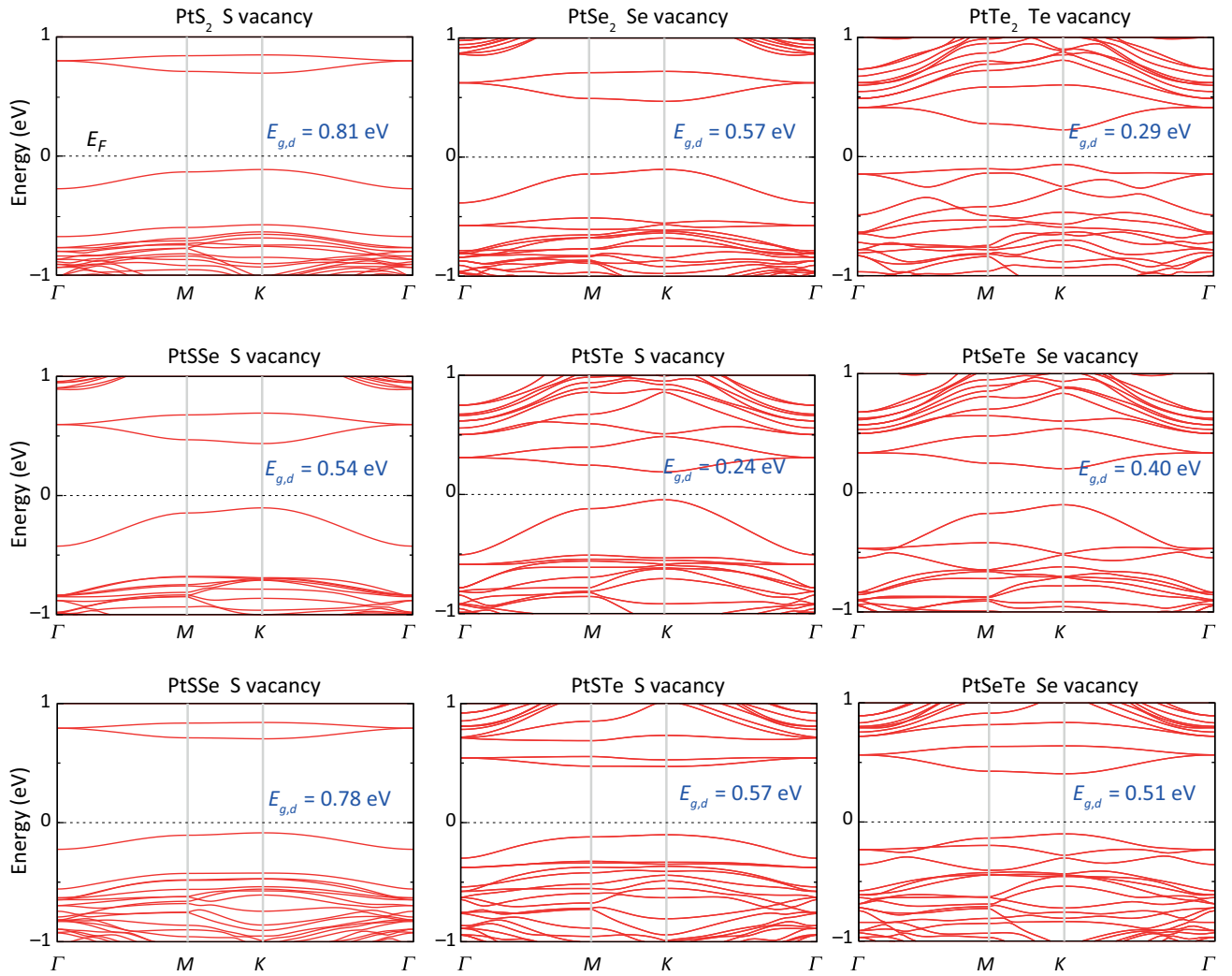


FIG. 16. Electronic-energy-band structures (PBE-functional calculations) for the single chalcogen vacancy included in the mono-layer PtX_2 and PtXY structures.

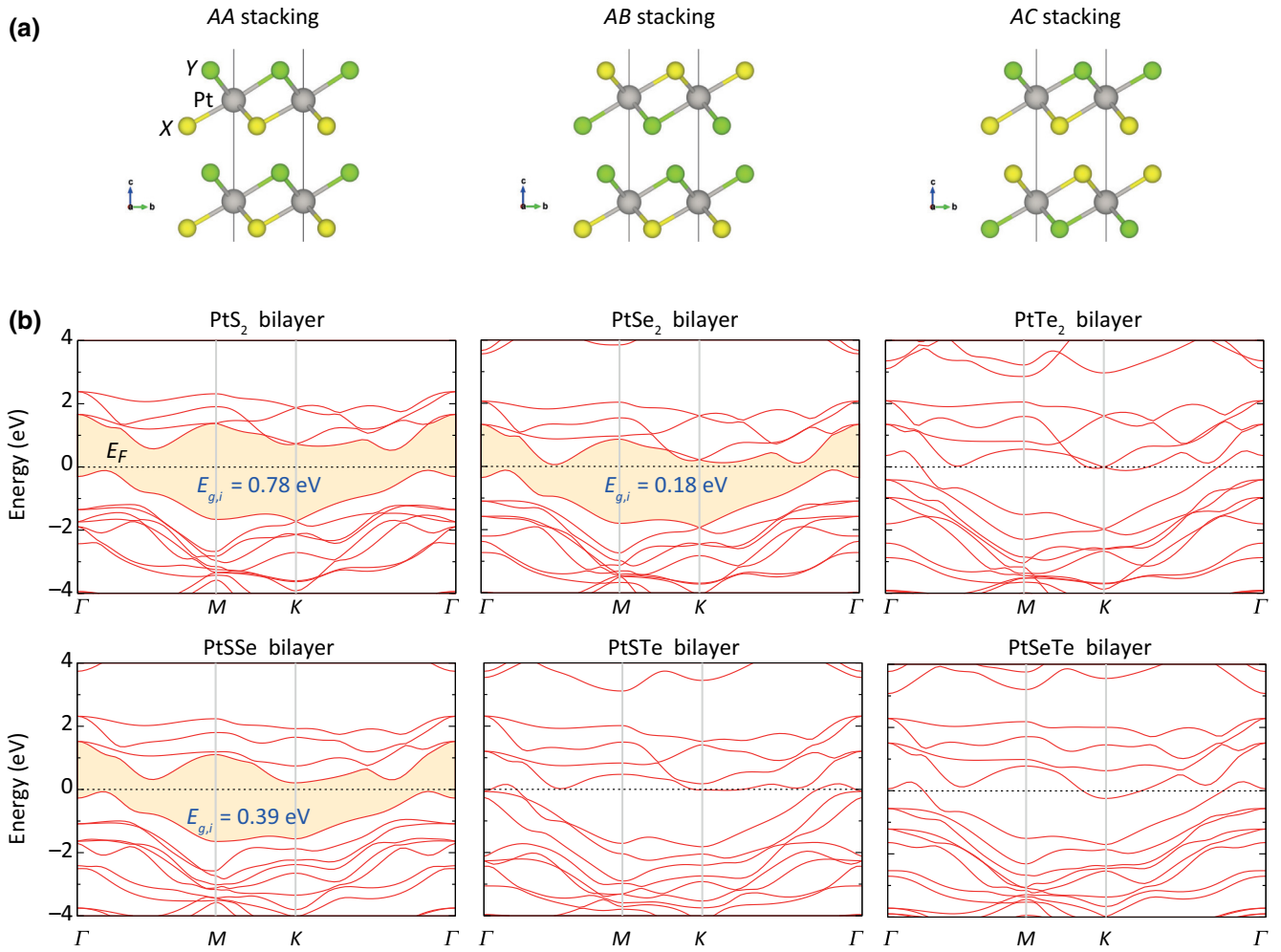


FIG. 17. (a) Considered types for stacking order of PtXY structures. (b) Electronic-energy-band structures (PBE-functional calculations) of the bilayer PtX₂ and PtXY structures.

calculations are performed by using PBE functional, using Hybrid functional may open the band gaps.

If we focus on the first $E_{\text{binding}}^{\text{bilayer}}$ values, we can say that bilayer PtS₂ has a weak vdW interaction between the layers, while the other binding mechanisms are a mixture of vdW and electrostatic interaction. The conduction and valence bands at the Fermi level show similar dispersion (compare Figs. 5 and 17), which hinders strong chemical interaction. Increase of the chalcogen row numbers leads to increase of the vertical distance between the layers and $E_{\text{binding}}^{\text{bilayer}}$ values. All bilayer structures containing Te atoms become semimetals and the band gaps of structures containing S and Se atoms are significantly reduced, similarly to other two-dimensional materials [65,66]. Another layer-layer interaction can be considered for vertical heterostructure of Janus PtXY structures. Interfacing these Janus PtXY monolayers with the other selected PtXY structures may tune the electronic structure and create a suitable band gap for the desired devices.

- [1] F. Ersan, S. Cahangirov, G. Gokoglu, A. Rubio, and E. Akturk, Stable monolayer honeycomb-like structures of RuX₂ (X=S, Se), *Phys. Rev. B* **94**, 155415 (2016).
- [2] E. Vatansever, S. Sarikurt, and R. F. L. Evans, Hysteresis features of the transition-metal dichalcogenides VX₂ (X = S, Se, and Te), *Mater. Res. Express* **5**, 046108 (2018).
- [3] Y.-P. Gao, X. Wu, K.-J. Huang, L.-L. Xing, Y.-Y. Zhang, and L. Liu, Two-dimensional transition metal diseleniums for energy storage application: A review of recent developments, *CrystEngComm* **19**, 404 (2017).
- [4] W. Choi, N. Choudhary, G. H. Han, J. Park, D. Akinwande, and Y. H. Lee, Recent development of two-dimensional transition metal dichalcogenides and their applications, *Mater. Today* **20**, 116 (2017).
- [5] V. Agarwal and K. Chatterjee, Recent advances in the field of transition metal dichalcogenides for biomedical applications, *Nanoscale* **10**, 16365 (2018).
- [6] E. Yang, H. Ji, and Y. Jung, Two-dimensional transition metal dichalcogenide monolayers as promising

- Sodium ion battery anodes, *J. Phys. Chem. C* **119**, 26374 (2015).
- [7] C. Ataca, H. Şahin, and S. Ciraci, Stable, Single-layer MX_2 transition-metal oxides and dichalcogenides in a honeycomb-like Structure, *J. Phys. Chem. C* **116**, 8983 (2012).
- [8] T. Brülle, A. Denisenko, H. Sternschulte, and U. Stimming, Catalytic activity of platinum nanoparticles on highly boron-doped and 100-oriented epitaxial diamond towards HER and HOR, *Phys. Chem. Chem. Phys.* **13**, 12883 (2011).
- [9] M. Bernardi, M. Palummo, and J. C. Grossman, Extraordinary Sunlight absorption and one nanometer thick photovoltaics using two-dimensional monolayer materials, *Nano Lett.* **13**, 3664 (2013).
- [10] M. Bernardi, C. Ataca, M. Palummo, and J. C. Grossman, Optical and electronic properties of two-dimensional layered materials, *Nanophotonics* **6**, 30 (2017).
- [11] F. Ersan, H. Ozyaydin, G. Gökoğlu, and E. Aktürk, Theoretical investigation of lithium adsorption, diffusion and coverage on MX_2 ($\text{M} = \text{Mo}, \text{W}$; $\text{X} = \text{O}, \text{S}, \text{Se}, \text{Te}$) monolayers, *Appl. Surface Sci.* **425**, 301 (2017).
- [12] T. L. Tan, M.-F. Ng, and G. Eda, Stable monolayer transition metal dichalcogenide ordered alloys with tunable electronic properties, *J. Phys. Chem. C* **120**, 2501 (2016).
- [13] P. Johari and V. B. Shenoy, Tuning the electronic properties of Semiconducting transition metal dichalcogenides by applying mechanical, *Strains ACS Nano* **6**, 5449 (2012).
- [14] S.-H. Su, W.-T. Hsu, C.-L. Hsu, C.-H. Chen, M.-H. Chiu, Y.-C. Lin, W.-H. Chang, K. Suenaga, J.-H. He, and L.-J. Li, Controllable synthesis of band-gap-tunable and monolayer transition-metal dichalcogenide alloys, *Front. Energy Res.* **2**, 27 (2014).
- [15] Z. Shi, Q. Zhang, and U. Schwingenschlögl, Alloying as a route to monolayer transition metal dichalcogenides with improved optoelectronic performance: $\text{Mo}(\text{S}_{1-x}\text{Se}_x)_2$ and $\text{Mo}_{1-y}\text{W}_y\text{S}_2$, *ACS Appl. Energy Mater.* **1**, 2208 (2018).
- [16] L.-Y. Gan, Q. Zhang, Y.-J. Zhao, Y. Cheng, and U. Schwingenschlögl, Order-disorder phase transitions in the two-dimensional semiconducting transition metal dichalcogenide alloys $\text{Mo}_{1-x}\text{W}_x\text{X}_2$ ($\text{X} = \text{S}, \text{Se}$ and Te), *Sci. Rep.* **4**, 6691 (2014).
- [17] V. Kiran, D. Mukherjee, R. N. Jenjeti, and S. Sampath, Active guests in the $\text{MoS}_2/\text{MoSe}_2$ host lattice: Efficient hydrogen evolution using few-layer alloys of $\text{MoS}_2(1-x\text{Se}_2x)$, *Nanoscale* **6**, 12856 (2014).
- [18] A.-Y. Lu, H. Zhu, J. Xiao, C.-P. Chuu, Y. Han, M.-H. Chiu, C.-C. Cheng, C.-W. Yang, K.-H. Wei, Y. Yang, Y. Wang, D. Sokaras, D. Nordlund, P. Yang, D. A. Muller, M.-Y. Chou, X. Zhang, and L.-J. Li, Janus monolayers of transition metal dichalcogenides, *Nat. Nanotechnol.* **12**, 744 (2017).
- [19] J. Zhang, S. Jia, I. Kholmanov, L. Dong, D. Er, W. Chen, H. Guo, Z. Jin, V. B. Shenoy, L. Shi, and J. Lou, Janus monolayer transition-metal dichalcogenides, *ACS Nano* **11**, 8192 (2017).
- [20] D. Er, H. Ye, N. C. Frey, H. Kumar, J. Lou, and V. B. Shenoy, Prediction of enhanced catalytic activity for hydrogen evolution reaction in Janus transition metal dichalcogenides, *Nano Lett.* **18**, 3943 (2018).
- [21] Y. Ji, M. Yang, H. Lin, T. Hou, L. Wang, Y. Li, and S.-T. Lee, Janus Structures of transition metal dichalcogenides as the heterojunction photocatalysts for water Splitting, *J. Phys. Chem. C* **122**, 3123 (2018).
- [22] M. Meng, T. Li, S. Li, and K. Liu, Ferromagnetism induced by point defect in Janus monolayer MoSSe regulated by strain engineering, *J. Phys. D: Appl. Phys.* **51**, 105004 (2018).
- [23] S.-D. Guo and J. Dong, Biaxial strain tuned electronic structures and power factor in Janus transition metal dichalcogenide monolayers, *Semicond. Sci. Technol.* **33**, 085003 (2018).
- [24] T. Hu, F. Jia, G. Zhao, J. Wu, A. Stroppa, and W. Ren, Intrinsic and anisotropic Rashba spin splitting in Janus transition-metal dichalcogenide monolayers, *Phys. Rev. B* **97**, 235404 (2018).
- [25] Y. Guo, S. Zhou, Y. Bai, and J. Zhao, Enhanced piezoelectric effect in Janus group-III chalcogenide monolayers, *Appl. Phys. Lett.* **110**, 163102 (2017).
- [26] W. Shi and Z. Wang, Mechanical and electronic properties of Janus monolayer transition metal dichalcogenides, *J. Phys.: Condens. Matter* **30**, 215301 (2018).
- [27] M. Yagmurcukardes, Y. Qin, S. Ozen, M. Sayyad, F. M. Peeters, S. Tongay, and H. Sahin, Quantum properties and applications of 2D Janus crystals and their superlattices, *Appl. Phys. Rev.* **7**, 011311 (2020).
- [28] A. Mogulkoc, Y. Mogulkoc, S. Jahangirov, and E. Durgun, Characterization and stability of Janus TiXY ($\text{X/Y} = \text{S}, \text{Se},$ and Te) monolayers, *J. Phys. Chem. C* **123**, 29922 (2019).
- [29] B. Akgenc, Intriguing of two-dimensional Janus surface-functionalized MXenes : An ab initio calculation, *Comput. Mater. Sci.* **171**, 109231 (2020).
- [30] L. Feng, G. Gao, P. Huang, X. Wang, C. Zhang, J. Zhang, S. Guo, and D. Cui, Preparation of Pt Ag alloy nanoisland/graphene hybrid composites and its high stability and catalytic activity in methanol electro-oxidation, *Nanoscale Res. Lett.* **6**, 551 (2011).
- [31] H. Liu, C. Song, L. Zhang, J. Zhang, H. Wang, and D. P. Wilkinson, A review of anode catalysis in the direct methanol fuel cell, *J. Power Sources* **155**, 95 (2006).
- [32] E. Kemppainen, A. Bodin, B. Sebok, T. Pedersen, B. Seger, B. Mei, D. Bae, P. C. K. Vesborg, J. Halme, O. Hansen, P. D. Lund, and I. Chorkendorff, Scalability and feasibility of photoelectrochemical H_2 evolution: The ultimate limit of Pt nanoparticle as an HER catalyst, *Energy Environ. Sci.* **8**, 2991 (2015).
- [33] B. Devadas and T. Imae, Hydrogen evolution reaction efficiency by low loading of platinumnanoparticles protected by dendrimers on carbon materials, *Electrochem. Commun.* **72**, 135 (2016).
- [34] Y. Wang, L. Li, W. Yao, S. Song, J. T. Sun, J. Pan, X. Ren, C. Li, E. Okunishi, Y.-Q. Wang, E. Wang, Y. Shao, Y. Y. Zhang, H.-t. Yang, E. F. Schwier, H. Iwasawa, K. Shimada, M. Taniguchi, Z. Cheng, S. Zhou, S. Du, S. J. Pennycook, S. T. Pantelides, and H.-J. Gao, Monolayer PtSe_2 , a new semiconducting transition-metal-dichalcogenide, epitaxially grown by direct Selenization of Pt, *Nano Lett.* **15**, 4013 (2015).
- [35] X. Chia, A. Adriano, P. Lazar, Z. Sofer, J. Luxa, and M. Pumera, Layered Platinum dichalcogenides (PtS_2 , PtSe_2 , and PtTe_2) electrocatalysis: Monotonic dependence on the chalcogen size, *Adv. Funct. Mater.* **26**, 4306 (2016).

- [36] U. Gupta, B. S. Naidu, U. Maitra, A. Singh, S. N. Shirodkar, U. V. Waghmare, and C. N. R. Rao, Characterization of few-layer 1T-MoSe₂ and its superior performance in the visible-light induced hydrogen evolution reaction, *APL Mater.* **2**, 092802 (2014).
- [37] M. Sajjad, N. Singh, and U. Schwingenschlögl, Strongly bound excitons in monolayer PtS₂ and PtSe₂, *Appl. Phys. Lett.* **112**, 043101 (2018).
- [38] P. Li, L. Li, and X. C. Zeng, Tuning the electronic properties of monolayer and bilayer PtSe₂ via strain engineering, *J. Mater. Chem. C* **4**, 3106 (2016).
- [39] W. Zhang, J. Qin, Z. Huang, and W. Zhang, The mechanism of layer number and strain dependent bandgap of 2D crystal PtSe₂, *J. Appl. Phys.* **122**, 205701 (2017).
- [40] P. Manchanda, A. Enders, D. J. Sellmyer, and R. Skomski, Hydrogen-induced ferromagnetism in two-dimensional Pt dichalcogenides, *Phys. Rev. B* **94**, 104426 (2016).
- [41] W. Zhang, H. T. Guo, J. Jiang, Q. C. Tao, X. J. Song, H. Li, and J. Huang, Magnetism and magnetocrystalline anisotropy in single-layer PtSe₂: Interplay between strain and vacancy, *J. Appl. Phys.* **120**, 013904 (2016).
- [42] G. Kresse and D. Joubert, From ultrasoft pseudopotentials to the projector augmented-wave method, *Phys. Rev. B* **59**, 1758 (1999).
- [43] J. P. Perdew, K. Burke, and M. Ernzerhof, Generalized Gradient Approximation Made Simple, *Phys. Rev. Lett.* **77**, 3865 (1996).
- [44] J. Heyd, G. E. Scuseria, and M. Ernzerhof, Hybrid functionals based on a screened Coulomb potential, *J. Chem. Phys.* **118**, 8207 (2003).
- [45] S. Grimme, Semiempirical GGA-type density functional constructed with a long-range dispersion correction, *J. Comput. Chem.* **27**, 1787 (2006).
- [46] H. J. Monkhorst and J. D. Pack, Special points for Brillouin-zone integrations, *Phys. Rev. B* **13**, 5188 (1976).
- [47] H. B. Schlegel, Optimization of equilibrium geometries and transition structures, *J. Comput. Chem.* **3**, 214 (1982).
- [48] G. Kresse and J. Furthmüller, Efficient iterative schemes for ab initio total-energy calculations using a plane-wave basis set, *Phys. Rev. B* **54**, 11169 (1996).
- [49] G. Kresse and J. Furthmüller, Efficiency of ab-initio total energy calculations for metals and semiconductors using a plane-wave basis set, *Comput. Mater. Sci.* **6**, 15 (1996).
- [50] A. Zunger, S.-H. Wei, L. G. Ferreira, and J. E. Bernard, Special Quasirandom Structures, *Phys. Rev. Lett.* **65**, 353 (1990).
- [51] A. van de Walle, Multicomponent multisublattice alloys, nonconfigurational entropy and other additions to the alloy theoretic automated toolkit, *Calphad* **33**, 266 (2009).
- [52] M. Topsakal, S. Cahangirov, and S. Ciraci, The response of mechanical and electronic properties of graphene to the elastic strain, *Appl. Phys. Lett.* **96**, 091912 (2010).
- [53] X.-J. Ge, K.-L. Yao, and J.-T. Lü, Comparative study of phonon spectrum and thermal expansion of graphene, silicene, germanene, and blue phosphorene, *Phys. Rev. B* **94**, 165433 (2016).
- [54] T. Li, Ideal strength and phonon instability in single-layer MoS₂, *Phys. Rev. B* **85**, 235407 (2012).
- [55] R. C. Cooper, C. Lee, C. A. Marianetti, X. Wei, J. Hone, and J. W. Kysar, Nonlinear elastic behavior of two-dimensional molybdenum disulfide, *Phys. Rev. B* **87**, 035423 (2013).
- [56] S. Bertolazzi, J. Brivio, and A. Kis, Stretching and breaking of ultrathin MoS₂, *ACS Nano* **5**, 9703 (2011).
- [57] D. Cohen-Tanugi and J. C. Grossman, Mechanical Strength of nanoporous graphene as a desalination membrane, *Nano Lett.* **14**, 6171 (2014).
- [58] Z. Kahraman, A. Kandemir, M. Yagmurcukardes, and H. Sahin, Single-layer Janus-type Platinum dichalcogenides and their heterostructures, *J. Phys. Chem. C* **123**, 4549 (2019).
- [59] M. M. Alyörök, Y. Aierken, D. Çakır, F. M. Peeters, and C. Sevik, Promising piezoelectric performance of Single layer transition-metal dichalcogenides and dioxides, *J. Phys. Chem. C* **119**, 23231 (2015).
- [60] A. Togo and I. Tanaka, First principles phonon calculations in materials science, *Scr. Mater.* **108**, 1 (2015).
- [61] W. Xinchun, M. Kazuhiko, T. Arne, T. Kazuhiro, X. Gang, M. Johan, D. Kazunari, and A. Markus, A metal-free polymeric photocatalyst for hydrogen production from water under visible light, *Nat. Mater.* **8**, 76 (2009).
- [62] J. M. Bolts and M. S. Wrighton, Correlation of photocurrent-voltage curves with flat-band potential for stable photoelectrodes for the photoelectrolysis of water, *J. Phys. Chem.* **80**, 2641 (1976).
- [63] R. Peng, Y. Ma, B. Huang, and Y. Dai, Two-dimensional Janus PtSSe for photocatalytic water splitting under the visible or infrared light, *J. Mater. Chem. A* **7**, 603 (2019).
- [64] X. Li, Z. Li, and J. Yang, Proposed Photosynthesis Method for Producing Hydrogen from Dissociated Water Molecules Using Incident Near-Infrared Light, *Phys. Rev. Lett.* **112**, 018301 (2014).
- [65] S. Tongay, J. Zhou, C. Ataca, K. Lo, T. S. Matthews, J. Li, J. C. Grossman, and J. Wu, Thermally driven crossover from indirect toward direct bandgap in 2D Semiconductors: MoSe₂ versus MoS₂, *Nano Lett.* **12**, 5576 (2012).
- [66] S. Yang, C. Wang, C. Ataca, Y. Li, H. Chen, H. Cai, A. Suslu, J. C. Grossman, C. Jiang, Q. Liu, and S. Tongay, Self-driven photodetector and ambipolar transistor in atomically thin GaTe-MoS₂ p-n vdW heterostructure, *ACS Appl. Mater. Interfaces* **8**, 2533 (2016).
- [67] A. Bakhtatou and F. Ersan, Effects of the number of layers on the vibrational, electronic and optical properties of alpha lead oxide, *Phys. Chem. Chem. Phys.* **21**, 3868 (2019).